RESEARCH ARTICLE | JUNE 07 2022

# Interaction of a shock train with inherent isentropic waves in a curved isolator

Li-hao He (贺理浩); Hao Chen (陈昊) ✉; Lian-jie Yue (岳连捷); ... et. al



*Physics of Fluids* 34, 066106 (2022)
https://doi.org/10.1063/5.0095277

Physics of Fluids ARTICLE scitation.org/journal/phf

# Interaction of a shock train with inherent isentropic waves in a curved isolator

Cite as: Phys. Fluids **34**, 066106 (2022); doi: 10.1063/5.0095277
Submitted: 9 April 2022 · Accepted: 26 May 2022 ·
Published Online: 7 June 2022



Li-hao He (贺理浩), Hao Chen (陈昊),[a] Lian-jie Yue (岳连捷), Qi-fan Zhang (张启帆), and Wan-nan Wu (邬婉楠)

## AFFILIATIONS

State Key Laboratory of High-Temperature Gas Dynamics, Institute of Mechanics, Chinese Academy of Sciences, Beijing 100190, China

[a]Author to whom correspondence should be addressed: chenhao@imech.ac.cn

## ABSTRACT

Shock-train transitions in simplified curved isolators are carefully studied by simulation. The results show the shock-train behavior is subject to the complex pressure field created by the duct deflection, eventually presenting five modes during a backpressure-varying process. Of them, the most special one is the abrupt shock-train leap. It appears as the leading shocks interact with an adverse pressure gradient and follows a different path after a reversal of the direction the backpressure takes, which causes a shock-train hysteresis. If the curvature increases, the leap phenomenon, together with the related hysteresis, grows in number and intensity. Analysis indicates the background pressure gradients stem from the inherent left-running expansion waves and right-running compression waves. They control alternately the near-wall flow state, provoking the cyclic changes in the pressure gradient sign. Unlike the former, the latter can enhance separation through a positive feedback mechanism, rendering the shock train highly sensitive to backpressure. This is why the leap occurs. Comparing with the previously reported shock-induced leap indicates that there is a marked similarity in their behaviors, suggesting the irrelevance of the occurrence of a leap to the category of incident waves. Nevertheless, a delay in the onset usually follows a compression-wave-typed leap, which reflects that there is a triggering threshold for an incident wave. Given the fact that no local separation is provoked by the compression waves, it is speculated that the threshold should lie below the criterion for causing a separation, as opposed to the impression from the previous research.



## NOMENCLATURE

| | |
|---|---|
| $C_f$ | Friction coefficient |
| $H$ | Height of the isolator, mm |
| $h$ | The height of arc off the bottom wall, mm |
| $L$ | Length of the isolator, mm |
| $L_e$ | Length of duct extension, mm |
| $M$ | Mach number |
| $M_{\text{exit}}$ | Mass-weighted average Mach number at the isolator exit |
| $\dot{m}$ | Mass flow rate at the unpressurized state, kg/s |
| $\dot{M}$ | Mass flow rate flowing through the isolator, kg/s |
| $p_b$ | Backpressure, Pa |
| $p_i$ | Freestream static pressure, Pa |
| $p_0$ | Freestream total pressure, Pa |
| $R$ | Curvature radius, mm |
| $T$ | Period of oscillations, ms |
| $T_0$ | Freestream total temperature, K |
| $t_1, t_2, t_3, t_4, t_5$ | Characteristic time, ms |
| $\Delta t$ | Time step, s |
| $\theta$ | Angle of deflection, ° |
| $\zeta$ | Throttling ratio |

### Abbreviations

| | |
|---|---|
| APG | Adverse pressure gradient |
| BSP | Bottom separation point |
| CFD | Computational fluid dynamics |
| FANS | Favre-averaged Navier–Stokes |
| FPG | Favorable pressure gradient |
| PR | Pressure ratio |
| TSP | Top separation point |

## I. INTRODUCTION

Scramjets are one of the few techniques to power hypersonic flight. Typically, a scramjet consists of an inlet, an isolator, a

combustor, and a nozzle. Of them, the isolator is an air duct placed between the inlet and combustor. Its crucial function is to cut off pressure disturbance released by combustion, thereby preventing the inlet from being unstarted.[1] Meanwhile, it plays a vital role in combustion mode transitions.[2,3] The core flow phenomenon in the isolator is the shock train. It features multiple shock waves interacting with boundary layers, involving many complex aerodynamic problems such as shock/boundary-layer interactions and shock/shock interference. Given the need for common engineering practice, previous attention has been largely devoted to the isolators of a simple style, i.e., straight isolators. Thanks to decades of research, their flow characteristics and relevant mechanisms have been basically clear.[4–7]

Nevertheless, application scenarios of scramjets are diversifying recently, and it is increasingly hard for straight isolators to be suitable all the time due to their structural inflexibility. For example, for a scramjet-powered missile, it is common to employ a layout that includes multiple inlets but one single combustor.[8] In that case, a deflection of isolators is necessary owing to the inevitable centerline mismatch between the inlets and combustor. That is to say, the isolators should be curved, smoothly or sharply (of which the latter can be basically considered an extreme case of the former). Similar situations could be found where an engine is designed in a complex multi-channel type like combined-cycle engines[9] or for a special purpose like stealth.[10] Compared with simple straight isolators, additional background waves are generated in curved isolators. Their coupling with the original flowfield may render the flow behavior much more complex, even distinct. As a result, the knowledge from straight isolators cannot be directly applied to curved cases. Under the circumstances, it is necessary to undertake targeted investigations.

In this paper, a study is conducted on a simplified type of curved isolator. The primary objective is to explore the shock-train behaviors affected by inherent isentropic waves (especially, the compression waves), which is, to the best of the authors' knowledge, a flow problem as yet unexplored despite the present extensiveness of research regarding shock trains. Considering the difficulty in visualizing isentropic waves through experiments, a FANS-based numerical approach is adopted to reach that target. The rest of this paper is organized as follows. First, a review of the literature is performed in Sec. II to show the recent progress in learning the effects of background waves. Second, the numerical method and its validation are introduced in Sec. III. Third, the shock-train characteristics during different backpressure-varying processes and the effects of the angle of isolator deflection are described in detail in Secs. IV and V, respectively. An in-depth analysis is then provided in Sec. VI to reveal the underlying mechanisms behind the background pressure field and the shock-train leap. The final part is a concise summary.

## II. LITERATURE REVIEW

Background waves are not unique to curved isolators. In fact, the incident shock stemming from the inlet lip can create a series of shock waves and expansion waves even in straight isolators and change the shock-train characteristics, which has been a research focus for the past decades.[11–15] One subtopic that attracted attention is the kinematic and dynamic characteristics of a shock train affected by background shocks. As for this problem, Tan *et al.*[16] first carried out a study and found that the pointing direction of leading shocks switched upwards and downwards repeatedly during the upstream propagation of the shock train. Another finding was that three unstable stages with substantial oscillations and four stable stages appeared alternately. It was also observed that the background shocks could increase the sustainable backpressure and decrease the shock-train length. Later, Xu *et al.*[17–19] found through numerical simulations that rapid forward movement of the shock train always occurred when the separation point surmounted a reflection point of background shocks. Based on the free interaction theory and one-dimensional analysis, Li *et al.*[20,21] developed a low-order model to characterize the dynamic motion of the shock train under the influence of complex background shocks. Huang *et al.*[22,23] further studied the interaction between the shock train and background shocks in a curved isolator integrated with an inlet. It was found that curvature had a significant impact on the interaction pattern. Hou *et al.*[24,25] experimentally studied the self-excited oscillations and forced oscillations of the shock train under the influence of background waves. Based on this, Wang *et al.*[26] studied the low-frequency characteristics of shock-train oscillations and analyzed the flow mechanism of several different types of oscillations.

Another subtopic that has placed considerable value on is the shock-train hysteresis caused by background shocks, which is a reflection of the path dependence of isolator flows on backpressure. Huang *et al.*[27] are among the earliest groups who reported the phenomenon. They performed a cold-flow experiment using a direct-connect facility and observed that the shock-train hysteresis phenomenon appeared under the disturbance of wedge when changing the throttling ratio or backpressure. Later, Jiao *et al.*[28] used numerical simulations to study the response of a shock train to downstream backpressure forcing in a scramjet inlet-isolator at the overspeed condition. Results showed that there was a clear hysteresis loop during the shock-train oscillation. Shi *et al.*[29] further confirmed the existence of hysteresis and provided more details: the positions of leading shocks, flow patterns, and the averaged velocity of the shock train were all different when the shock train moved along opposite paths. Huang *et al.*[30] used a specially designed slope device to generate background shocks and studied the shock-train characteristics with cyclic variations in backpressure. They found that a hysteresis would occur when the shock train interacts with the large-scale wake zone downstream of the slope. They also studied the influence of slope sizes on hysteresis. Recently, Li and Chang[31] analyzed the hysteretic behaviors of separation shock caused by the shock-wave/boundary-layer interaction in the isolator with incident shocks. They found that the nonlinear relationship between the flow condition and the length of the shock system offered a dual solution to the pressure distribution, which resulted in the hysteresis of the separation shock.

By far, extensive studies have been conducted to uncover the effects of background shocks on shock trains, particularly for straight isolators. It has been already clear that strong shock waves can alter the isolator flow significantly in both the steady and dynamic aspects. Moreover, flow separations following the extra shocks can trigger shock-train hysteresis, which is unfavorable to engine control and performance. Those achievements provide a good foundation for understanding the flows of shock-affected isolators, but shocks are not the only type of background wave that a curved isolator may face. When the inlet is well designed and operates in the vicinity of the design point, the shock waves inside the inlet are very weak due to a fine reflection-eliminating design of the inlet shoulder. In this case, the primary subject in the background of a curved isolator (especially one

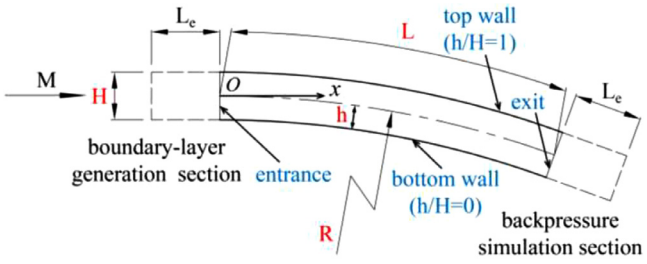


FIG. 1. Schematic diagram of the curved isolator.

with a small curvature) is likely to be isentropic compression and expansion waves generated by the isolator itself rather than shocks from the upstream inlet. Due to the natural dispersion, compression waves easily have a relatively weak pressure gradient but a relatively broad field of influence, as compared with a shock under the same condition. Predictably, those physical differences may cause obvious changes in shock-train characteristics, which make the isolator flows affected by autogenic isentropic waves—an important and interesting topic that remains to be explored.

## III. METHODOLOGY

### A. Description of isolator models

To isolate the effects of duct bending from other factors, a simplified two-dimensional curved isolator is designed according to the configuration in Ref. 22, as shown in Fig. 1. The origin of the coordinate system is positioned at the center of the isolator entrance. The top and bottom walls are concentric arcs, which ensures that the duct height ($H$) remains unchanged. Aside from the main body, the computational domain is extended by 1.4 times the height (i.e., $L_e = 1.4H$) in both directions, as outlined by dotted lines in Fig. 1. The downstream extension is utilized to eliminate the unphysical disturbance caused by setting the outlet boundary condition, whereas the upstream counterpart serves as a boundary-layer generator to simulate the incoming boundary layer. Since the focus of this study is on the influence of autogenic isentropic waves, only a thin boundary layer is considered here. Specifically, the consequent boundary-layer thickness is about 6.4% of the half-height of the isolator.

The size of a curved isolator described above is determined by three geometric parameters: height ($H$), the arc length of the centerline ($L$), and the radius of the centerline ($R$). For a scientific and convenient description, parameters, $L/H$ and $\theta = L/R \times 180/\pi$, are adopted hereinafter in place of the latter two, respectively. Table I summarizes the specific sizes of the isolators to be tested. Of them, case I is the baseline model for the current study. It refers to Ref. 32 on the selection of the length and height, except that a scaling up is conducted. Cases II and III are isolators with different angles of deflection. Together with case I, they roughly represent three categories of curvature that a curved isolator may fit into, in practice, specifically, the small curvature, medium curvature, and large curvature. In addition, there are another three cases that differ in angle or length (cases IV–VI), and they are included to test some hypotheses about the isolator flows, which will be detailed later.

TABLE I. Design parameters of curved isolators.

| Geometric parameters | Case I | Case II | Case III | Case IV | Case V | Case VI |
|---|---|---|---|---|---|---|
| $H$, mm | 70 | 70 | 70 | 70 | 70 | 70 |
| $L/H$ | 7.1 | 7.1 | 7.1 | 14.3 | 14.3 | 7.1 |
| $\theta$, ° | 20 | 10 | 30 | 20 | 40 | 60 |

### B. Numerical method and validation

#### 1. Description of the numerical approach

An unsteady CFD method is adopted to obtain the shock train characteristics, considering the possible flow unsteadiness. The solver is integrated in the software package from Ansys Fluent® and based on the two-dimensional Favre-averaged Navier–Stokes (FANS) equations. In calculating the flowfield, the turbulence is modeled by the $k$–$\omega$ Shear Stress Transport (SST) model, which is frequently used for investigations of inlet or isolator flows[20,21,33,34] due to its good behavior in adverse pressure gradients (APGs).[35] The fluid is processed as thermally perfect air, and the piecewise polynomial method is utilized to compute the specific heat. Meanwhile, the viscosity coefficient is calculated by the Sutherland formula. As for the difference scheme, the Roe Flux-Difference Splitting (Roe-FDS) scheme is used for vector flux splitting. A second-order upwind scheme is used for the flow term, and a first-order upwind scheme for the turbulent kinetic energy term and specific dissipation rate term. The time step of unsteady simulations is set at $10^{-6}$ s, which is lower than the characteristic time estimated according to the minimum grid size and freestream velocity. A second-order implicit scheme is adopted to advance the transitional formulation. In addition, the flow rate and mass-averaged Mach number at the outlet are monitored during calculations along with the residuals. The criterion for convergence is that the monitored parameters remain unchanged, and the residuals decrease below $10^{-6}$.

The computational domain is filled with a structured mesh, and the near-wall cells are, in particular, refined to ensure that the great majority of $y^+$ values are kept below one. Figure 2 displays the computational mesh, and for clarity, the cell number is reduced to 1/16 of the real one. During simulations, the boundary conditions of the computational entrance and exit are set as the pressure inlet and pressure outlet, respectively, and meanwhile, the walls are treated as adiabatic. For all isolator cases, the incoming total pressure $p_0$ is 101 325 Pa, the total temperature $T_0$ is 300 K, and the Mach number $M$ is 3.0.

#### 2. Code validation regarding time-averaged flow prediction

The verification is implemented through comparisons between public experimental data and the numerical results obtained

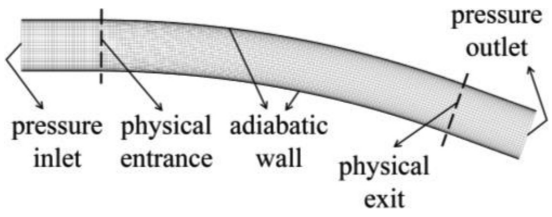


FIG. 2. Illustration of computational mesh and boundary conditions.

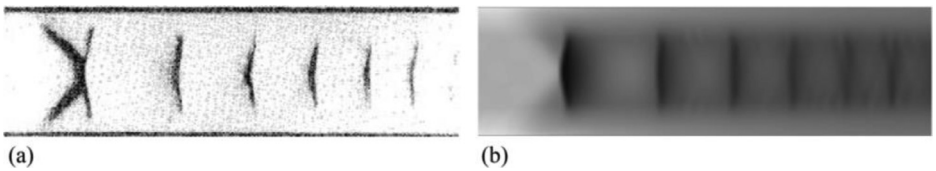


FIG. 3. Comparison between (a) the experimental images from Ref. 36 and (b) the present numerical results. [Image reproduced with permission from B. F. Carroll and J. C. Dutton, J. Propul. Power **6**(2), 186–193 (1990). Copyright 1989 American Institute of Aeronautics and Astronautics, Inc.]

correspondingly from the above-mentioned approach. It involves two aspects: shock-train structure and pressure distribution. Details are as follows.

*a. Example 1: Shock-train structure in a straight isolator.* The data for validation come from the wind tunnel experiment by Carroll and Dutton.[36] The test article is a straight isolator, which is 32.06 mm high and 754 mm long. The incoming Mach number is 1.6, the total pressure is 207 kPa, and the ratio of the incoming boundary-layer thickness to the half of the isolator height is 0.08. Figure 3 compares the numerical and experimental schlieren images of the shock-train pattern. It can be observed that the calculated leading shocks are quite similar to the experimental counterpart from the perspectives of the bifurcation shape and the shock position. Also, good agreement can be found in the number of the subsequent shocks and the spacing distance between any two of them.

*b. Example 2: Wall pressure distribution in a straight isolator.* In the experiment by Kawatsu *et al.*,[37] the model is also a straight isolator. The height of the isolator is 30 mm, and its length is 290 mm. The incoming Mach number is 2.3, the total pressure is 100 kPa, the total temperature is 298 K, and the ratio of backpressure to the incoming static pressure is 3.8. Figure 4 presents the comparison between the calculated and experimental pressure distributions, where the x-axis is the dimensionless length and the y-axis is the pressure ratio based on the incoming total pressure. It can be seen that the curve obtained by simulation basically agrees with that of the experiment, including the starting point of the pressure jump, which suggests the position of the leading shock.

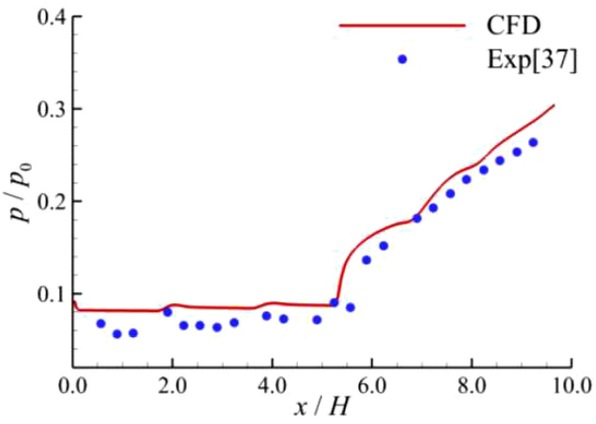


FIG. 4. Comparison between experimental[37] and numerical pressure distributions.

The foregoing two examples indicate that the numerical approach employed herein can offer good prediction of the time-averaged characteristics of isolator flow.

## 3. Code validation regarding dynamic flow prediction

The capability of describing unsteady flow is examined with the test in Ref. 38, which portrays an inlet being about to transit from a started state to an unstarted state. The test Mach number is 4.9, the freestream static pressure is 5.38 kPa, and the total temperature is 333 K. With these conditions, simulation has been performed, and the results are exhibited in Figs. 5 and 6. As can be seen from the flowfield snapshots, there is no great disparity between the experiment and calculation at any moment. The existence of several minor differences may originate from the reduction in model dimension from being rectangular to two-dimensional. Further comparison of the instantaneous pressure distributions confirms their basic similarity in the shock-train structures. These indicate that the numerical approach described above will have good predicting precision if the macroscopic flow unsteadiness exists.

Additionally, a frequency validation is conducted to further validate the capability of the present numerical approach in predicting the unsteady flow features based on the test data from Li *et al.*[39] The test freestream Mach number is 5.9, the total pressure is 1.27 MPa, and the total temperature is 810 K. Table II presents the comparison between the experiment and simulation in terms of dominant buzz frequencies. It can be seen that their results are very close at the throttling ratio of

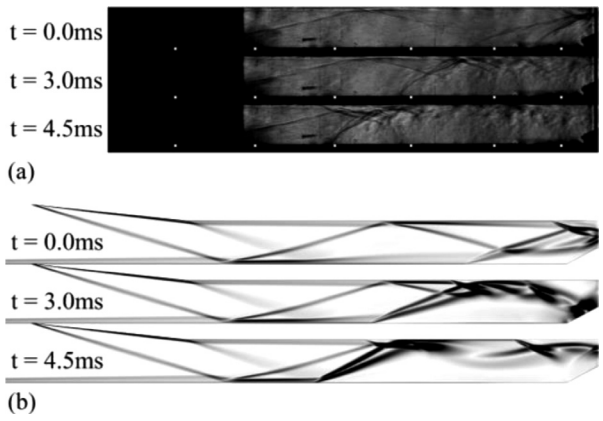


FIG. 5. Comparison between (a) the experimental images from Wagner *et al.*[38] and (b) the present numerical results. [Image reproduced with permission from Wagner *et al.*, AIAA J. **47**(6), 1528–1542 (2009). Copyright 2009 Authors, licensed under a Creative Commons Attribution 4.0 License].

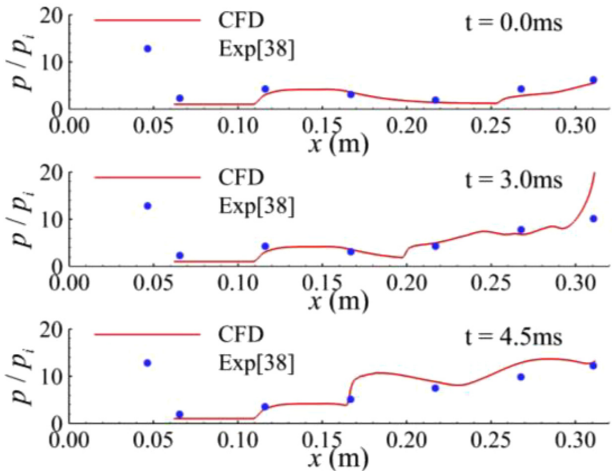


FIG. 6. Comparison between experimental[38] and numerical pressure curves at typical moments.

0.6, and agreement becomes even better when it comes to 0.7. As for the predicting errors, they possibly originate from the model simplification from a three-dimensional structure to a two-dimensional one. Anyhow, the good coincidence proves that the numerical method described above can be used as a tool to analyze unsteady flows.

### 4. Grid sensitivity analysis and time step sensitivity analysis

To validate the grid convergence, three grids of different spatial resolutions (termed as a coarse grid, a fine grid, and a dense grid, respectively) are constructed with the height of the first layer unchanged. The corresponding numbers are $9.52 \times 10^4$, $1.93 \times 10^5$, and $2.55 \times 10^5$, respectively. For each of these grids, the $y^+$ is mostly lower than one. The analysis is carried out at a freestream Mach number of 3.0 and a typical backpressure ratio ($p_b/p_i$, denoted by PR) of 4.0. To show the tendency, the calculated pressure distributions along the bottom wall are compared in Fig. 7. It can be seen that the curves from the fine and dense grids are in good agreement, while the coarse case is different in the region after the pressure jump. It suggests that the simulation is convergent once the cell number exceeds that of the fine grid. Therefore, to save computing resources, the fine grid is used for the baseline model (case I). As for isolators of different parameters, the number of cells is adjusted according to keep the spatial resolution approximately constant.

Moreover, to examine the convergence of the time step, three cases of increasing time resolutions ($1 \times 10^{-5}$, $5 \times 10^{-6}$, and $1 \times 10^{-6}$ s) have been calculated at a typical backpressure state (PR = 4.0). As shown in Fig. 8, a small change occurs when the time

TABLE II Comparison between experimental[39] and numerical buzz frequencies.

| Throttling ratio | Experimental frequency (Hz) | Numerical frequency (Hz) | Relative error |
|---|---|---|---|
| 0.6 | 374 | 400 | 6.95% |
| 0.7 | 400 | 403 | 0.01% |

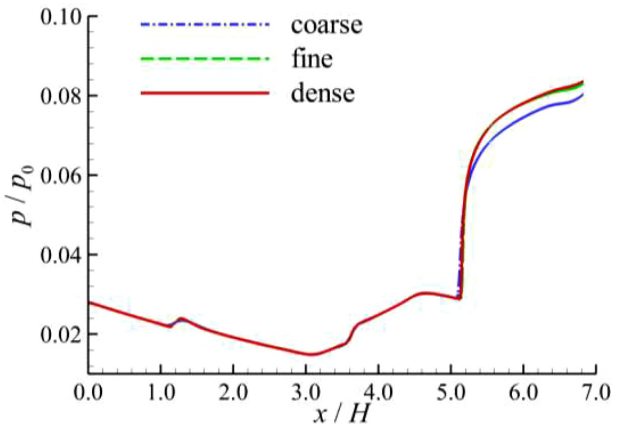


FIG. 7. Pressure distributions along the bottom wall ($h/H = 0$) from grids of different spatial resolutions (PR = 4.0).

step decreases from $1 \times 10^{-5}$ to $5 \times 10^{-6}$ s. In contrast, there is no discernible difference between two cases with smaller time steps, no matter how the flowfield changes. It suggests that the time step should be kept below $5 \times 10^{-6}$ s in order to obtain an accurate result; $1 \times 10^{-6}$ s, which is adopted by the current study, is a proper choice.

## IV. TYPICAL SHOCK-TRAIN BEHAVIORS AFFECTED BY ISENTROPIC WAVES

To gain an overall impression as to how a shock train behaves in a curved isolator, an elaborate study is carried out on the baseline configuration (case I) with both the backpressure-rising and -dropping processes considered. In adjusting the backpressure upwards or downwards, a fixed-step strategy is applied: the variation per step is set at a tenth of the freestream static pressure, i.e., $\Delta p = \pm 0.1 p_i$. The time interval between two changes is normally 0.04 s, which is sufficient for the convergence of flowfields to a steady state. If oscillations appear,

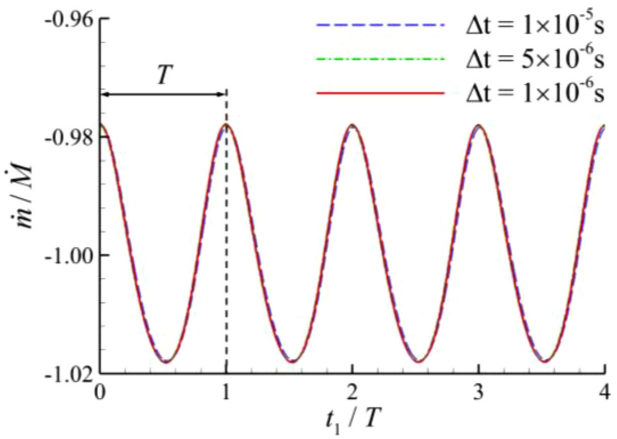


FIG. 8. Curves of mass flow rate flowing through the isolator ($\dot{M}$) for cases of different time resolutions (case I, PR = 4.0). $T$ denotes the oscillatory period, equaling 4.4 ms here. $\dot{m}$ represents the mass flow rate at the unpressurized state, i.e., 3.89 kg/s. The zero point of the time $t_1$ corresponds to the moment of the first peak of periodic oscillations at PR = 4.0.

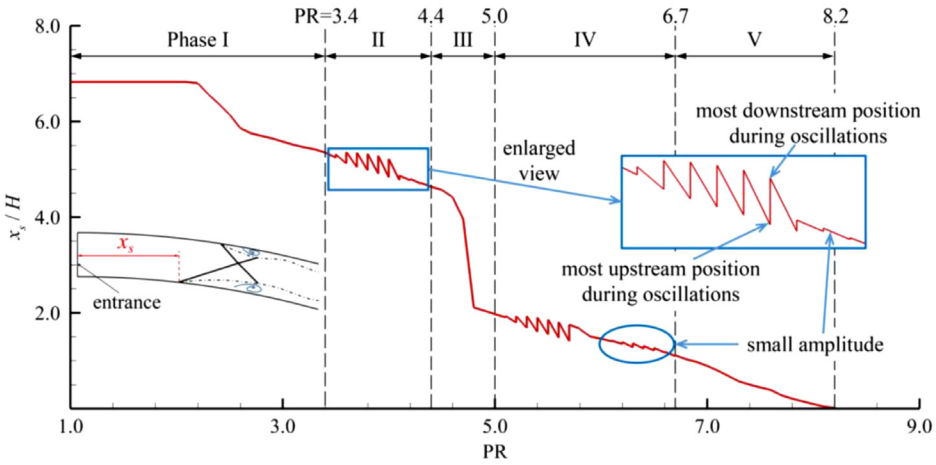


Phase I: The appearance of leading shocks; II: Oscillations with a slightly asymmetric shock pattern; III: The forward leap; IV: Oscillations with an extremely asymmetric shock pattern; V: Smooth movements

**FIG. 9.** Positional variations of the leading shock along the bottom wall ($h/H = 0$) during the whole backpressure-rising process (case I, $1 \leq \mathrm{PR} \leq 8.2$).

the time will be doubled so that key dynamic attributes can be learned. Given that the focus of this study is on the interaction between the shock train and isentropic waves, the maximum backpressure tested herein is when the shock train just touches the isolator entrance; higher values that can expel the shock train and cause unstart are temporarily set aside. To refer to the backpressure state conveniently, the abbreviation, PR, is adopted hereinafter for the ratio of backpressure to incoming static pressure (i.e., $p_b/p_i$). The following is a detailed description of the evolution of the shock train.

### A. Backpressure-rising process

According to the shock-train characteristics, the backpressure-rising process can be roughly divided into five phases, as shown in Fig. 9, namely, the appearance of leading shocks, oscillations with a slightly asymmetric shock pattern, the forward leap, oscillations with an extremely asymmetric shock pattern, and smooth movements. Their respective features are as follows.

#### 1. Phase I: The appearance of leading shocks ($1 < \mathrm{PR} \leq 3.4$)

Figure 10 presents the Mach number contours and the numerical schlieren of the isolator under the unpressurized condition. For clarity, sections for boundary-layer generation and backpressure simulation are not included here. It can be seen that isentropic waves are densely emitted from two walls. They are interlaced in the isolator, forming a complex background flowfield. From the pressure curves exhibited in Fig. 11 (where $h/H = 0$ represents the bottom wall and $h/H = 1$ represents the top wall), neither the compression-typed waves nor the expansion-typed waves can always prevail even in the near-wall

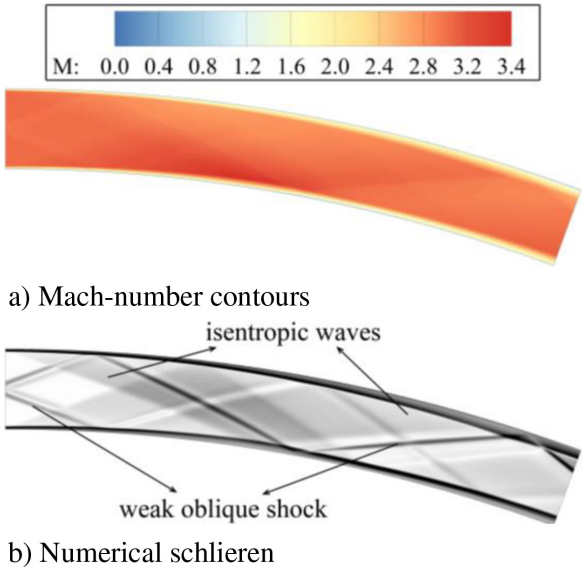


**FIG. 10.** Unpressurized flow pattern of the baseline isolator (case I).

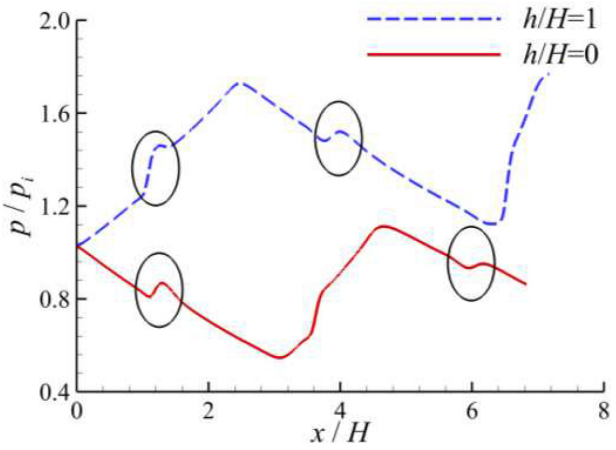


**FIG. 11.** Wall-pressure distributions of the unpressurized isolator (case I). The small turnings circled by black lines are caused by two weak shocks and their reflections, which originate from the boundary layer growth near the entrance.

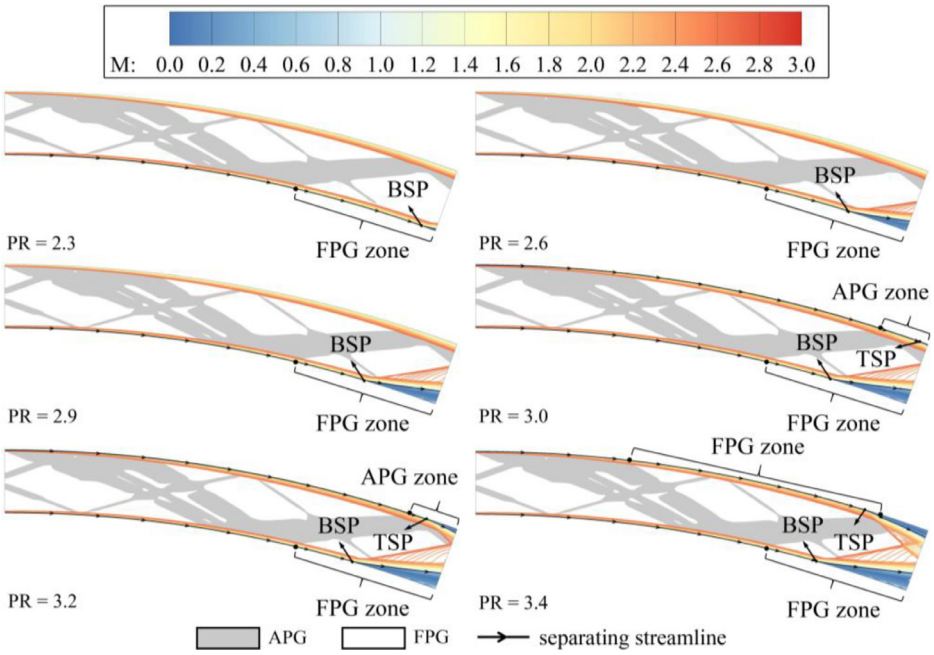


**FIG. 12.** Formation process of leading shocks (case I, phase I, $1 < PR \leq 3.4$). Gray areas are where the sign of the streamwise pressure gradient in the background is positive, and the white are where negative.

regions. Instead, they combine to make the pressure rise and fall alternately along the duct, which shows a case distinct from the flow over a single curved wall or through a straight isolator.[4] For convenience, a near-wall region where the pressure grows streamwise is termed the APG zone (adverse pressure gradient zone), whereas one featuring a local pressure decrease is termed the FPG zone (favorable pressure gradient zone). By the way, two weak oblique shocks are formed near the entrance due to the boundary layer developing along the walls. The shocks and their reflections cause several small turnings of pressure curves (circled in Fig. 11) but do not alter the general trend.

As the backpressure increases, the shock train gradually comes into being. The initial appearance occurs on the bottom wall at the PR of 2.3, as shown in Fig. 12 where a sign of flow separation can be detected. Then the separation expands upstream with increasing backpressure, and meanwhile, the separation-induced shock, which is also the bottom branch of the shock-train leading shocks, becomes visible and moves accordingly. It is not until the PR reaches 3.0 that the top branch starts to appear. After the appearance, it shifts and grows rapidly with the upstream expansion of the top separation, while the bottom branch hardly changes at the same time. When the PR arrives at 3.4, the head structure of the shock train takes shape, presenting a flow pattern characterized by two separation bubbles and a pair of crossed oblique shock waves. Combining Fig. 12 with Fig. 11, it is found that the top separation point (abbreviated as TSP in images) crosses over an APG zone into an FPG zone during this phase, whereas the bottom separation point (abbreviated as BSP in images) stays in the FPG zone where it starts all the time.

### 2. Phase II: Oscillations with a slightly asymmetric shock pattern ($3.4 < PR \leq 4.4$)

When the PR is raised to 3.5, the isolator flowfield turns unstable and self-excited oscillations are activated. After that, the oscillatory state continues till the PR gets to 4.4. During this period, the amplitude of oscillations roughly increases first and then decreases with the backpressure. The tendency of the oscillatory frequency is opposite, but the difference between the maximum and minimum values (236 and 227 Hz) is marginal. In the subsequent paragraph, the case at the PR of 4.0 is taken as an example to introduce the shock-train characteristics within this phase.

Figure 13 shows the time-varying curve of the exit Mach number at PR = 4.0. From it, periodic shock-train oscillations can be found, possessing a frequency of about 230 Hz. In a typical cycle, it is observed that the separation zone on either side varies in the location and size (Fig. 14). As a result, the shock train shifts back and forth, synchronously. Since the amplitude is mild, the basic shock pattern stays the same, featuring a pair of leading shocks of slight asymmetry. To describe the shock movement

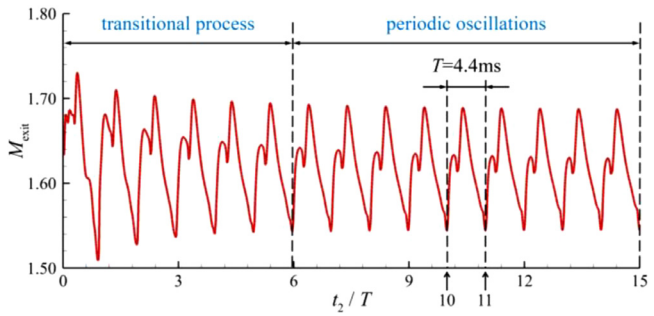


**FIG. 13.** Time-varying curve of the exit Mach number at PR = 4.0 (case I, phase II). $M_{exit}$ represents the mass-weighted average Mach number at the exit of the isolator. $T$, which denotes the oscillatory period, is 4.4 ms here. The zero point of the time $t_2$ corresponds to the moment when the PR just changes to 4.0.

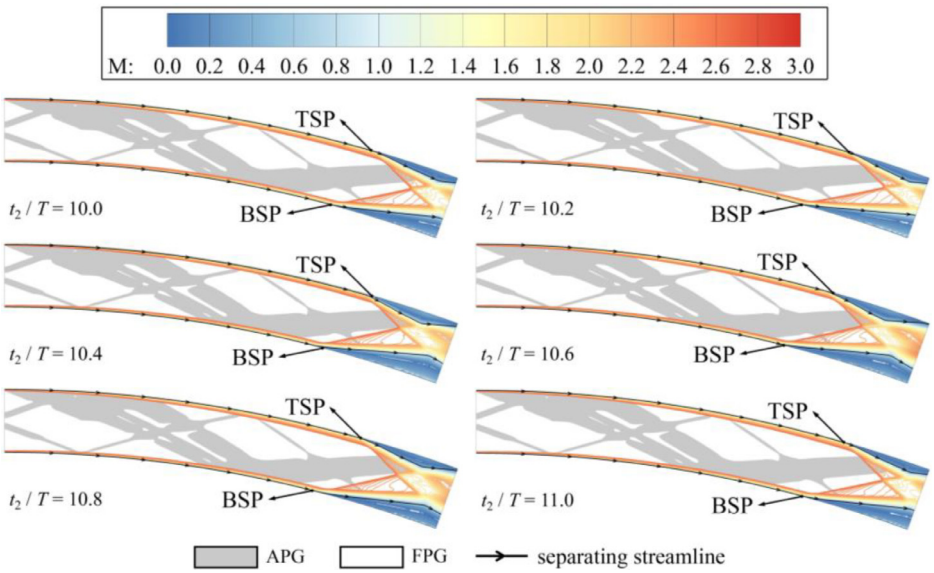


**FIG. 14.** Transient flow patterns in a typical oscillation cycle (case I, phase II, PR = 4.0, $10.0 \leq t_2/T \leq 11.0$).

more clearly, trajectories of the shock foots are further extracted in Fig. 15. It can be seen that there is no big difference in the oscillatory amplitude between the two leading shocks, and yet they have a phase difference with the result that the top branch always lags behind the bottom. However, the lag is so small that the shock train can be regarded as oscillating as a whole.

Additionally, there is an interesting detail that regards the second phase. Figure 16 shows the flow patterns at the start and the end of the second phase, and since oscillations at two boundaries are pretty weak and barely discernible in images, only a picture is given as a representative for each case. From that, it is easy to know that both separation points stay in their respective FPG zones created by background waves all along. Furthermore, the second phase starts with a situation where the top separation point just enters the FPG zone and ends when the bottom separation point is about to leave the FPG zone. This behavior implies a strong connection between the appearance of the second phase and the interaction with FPGs from two sides.

### 3. Phase III: The forward leap ($4.4 < PR \leq 5.0$)

When the PR exceeds 4.4, the unsteadiness vanishes, and the shock train switches to a unique flow regime. As can be seen in Fig. 17, gentle forward transitions of the shocks and separations occur first in the post-oscillation period (PR = 4.5–4.7). Surveying the shock

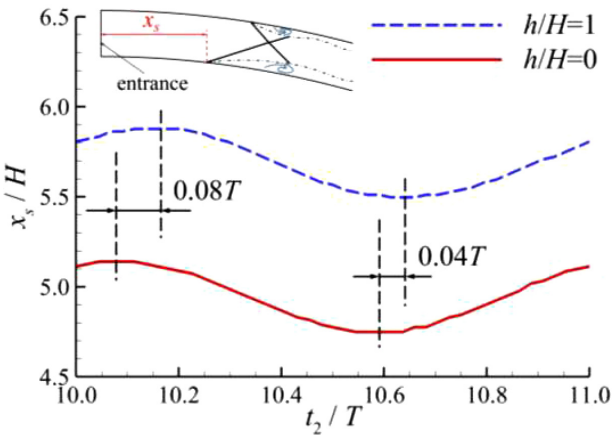


**FIG. 15.** Positional variations of leading shocks along isolator walls in a typical oscillation cycle at PR = 4.0 (case I, phase II). $T$, which denotes the oscillatory period, is 4.4 ms here. The zero point of the time $t_2$ corresponds to the moment when the PR just changes to 4.0. To obtain the shock positions, the wall-pressure distributions are obtained first, and then the contrasting edges that denote the shock foots are extracted.

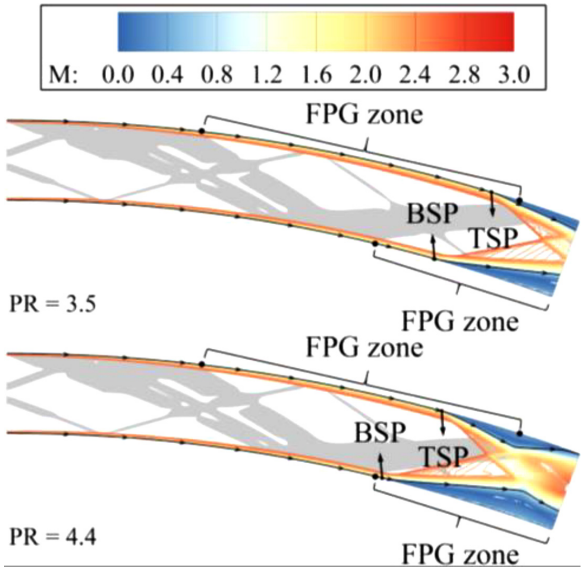


**FIG. 16.** Flow patterns at PRs of 3.5 and 4.4 (case I, phase II).

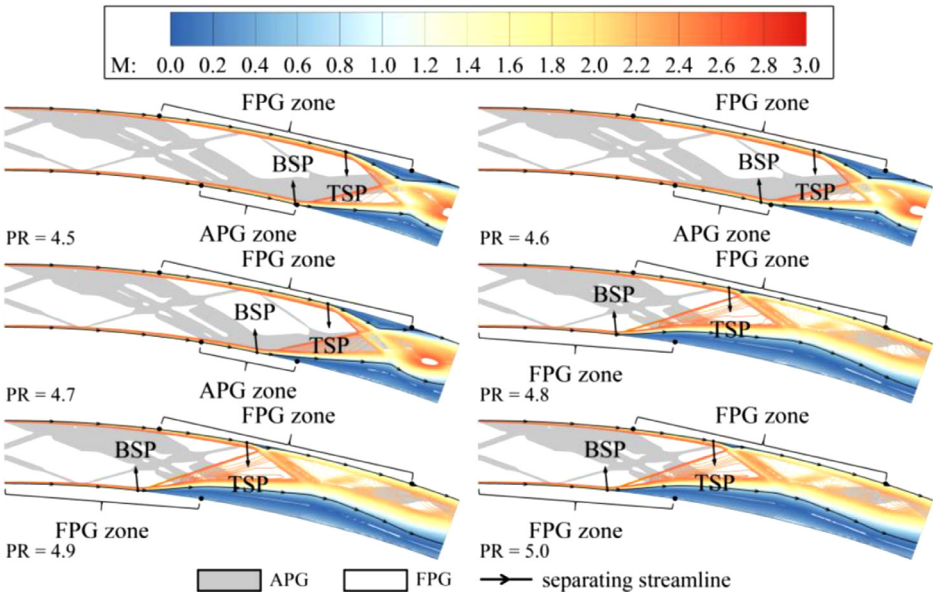


FIG. 17. Flow evolution during the shock-train leap (case I, phase III, $4.4 < PR \leq 5.0$).

behaviors at this stage, it seems that the top branch is almost unmoved, while the pace of the bottom tends to increase. A gradual transformation from an FPG zone to an APG zone is also spotted in the flow environment where the bottom shock stands. Then a significant change takes place. As the PR is raised to 4.8, the bottom separation expands rapidly and considerably. Meanwhile, the adjacent shock makes a giant leap forward, completely out of the APG zone it just got into. In contrast, the top shock hardly moves and still lies in the FPG zone where it has already been since the end of the first phase. In this way, the discrepancy in distance between two leading shocks increases markedly. Moreover, the greatly enlarged bottom separation presses the supersonic core flow forcefully against the top wall, which causes a nearly total suppression of the top separation bubble. Consequently, the shock train turns extremely asymmetric in an instant. Thereafter, the shock train resumes shifting upstream smoothly until the next phase begins; just that the flow pattern is no longer the same as before.

To further reveal the shock-train characteristics in the leaping process (PR = 4.7–4.8), coordinates of the leading shocks are recorded at an interval of 1 ms, as shown in Fig. 18, where the zero second denotes the moment when the PR becomes 4.8. It can be seen that although both the distance and the velocity are different between the shocks from two sides, the ways they transfer are similar and synchronized. They both start with a period of rapid forward movement and then oscillate mildly and convergently. Aside from that one may notice that the speed at which the bottom shock advances is roughly stationary ($t_3/T = 1.0$–$12.0$).

### 4. Phase IV: Oscillations with an extremely asymmetric shock pattern ($5.0 < PR \leq 6.7$)

Once the PR rises beyond 5.0, the shock train loses its stability again until the PR passes 6.7. Compared with the second phase, the new instability has two differences. First, the shock train here inherits the extremely asymmetric shock structure from the third phase (as shown in Fig. 19 where the cases at PRs of 5.4 and 6.4 are cited as examples), which shows a striking contrast with the previous. Second, the oscillatory frequency varies with the backpressure from 120 to 160 Hz (see examples in Fig. 20), much lower than the preceding counterpart. However, these two phases are quite similar in the tendency of the oscillatory amplitude—that is to say, their amplitudes basically both increase first and then gradually decrease to a very low level with increasing backpressure. In addition, it can be learned from Fig. 21 that while the instability is happening, the separation points on both sides stand in the FPG zones from beginning to end, which also agrees with the observation of the second phase.

### 5. Phase V: Smooth movements ($6.7 < PR \leq 8.2$)

When the PR exceeds 6.7, the shock train returns to steadiness and the last flow phase starts. As shown in Fig. 22, the top separation

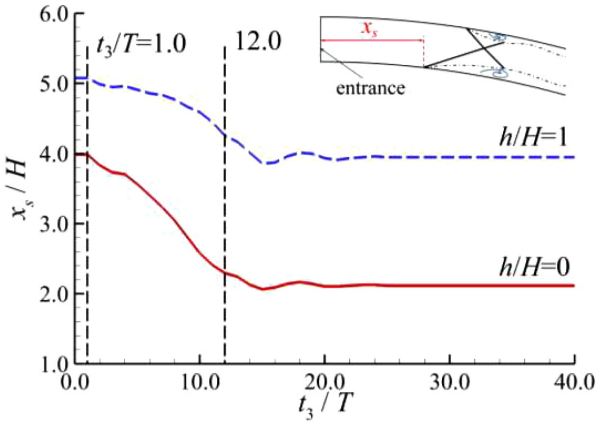


FIG. 18. Positional variations of leading shocks after PR increases from 4.7 to 4.8 (case I, phase III). $T$ is artificially set at 1.0 ms for reference due to the inexistence of periodic oscillations at this stage. The zero point of $t_3$ corresponds to the moment when the PR just changes to 4.8.

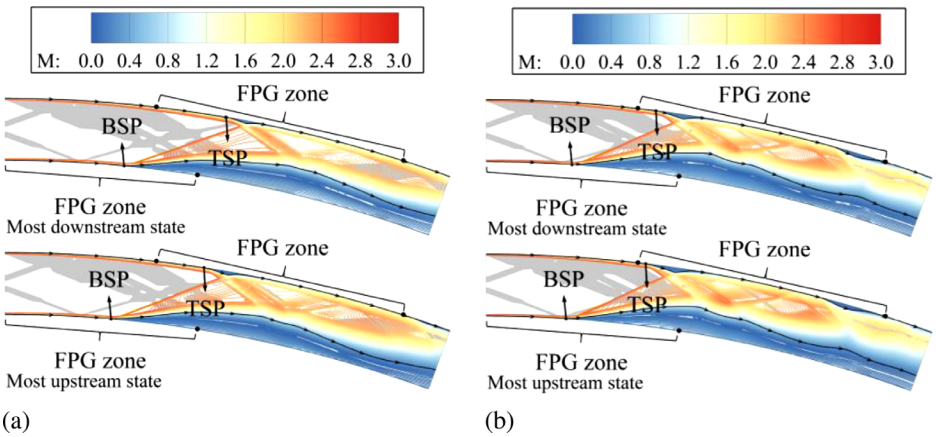


**FIG. 19.** Oscillatory patterns at (a) PR = 5.4 and (b) PR = 6.4 within the fourth phase (case I).

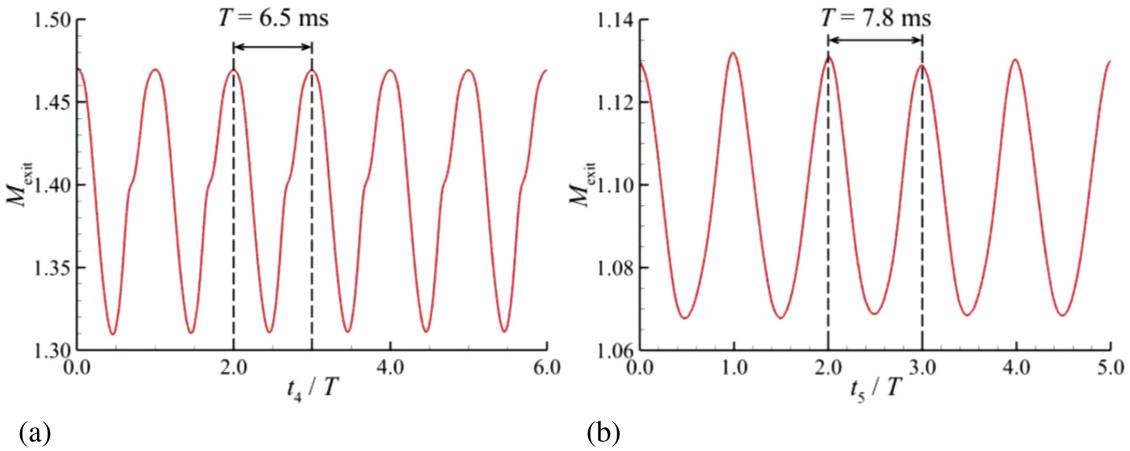


**FIG. 20.** Time-varying curves of the exit Mach number at (a) PR = 5.4 and (b) PR = 6.4 (case I, phase IV). $M_{exit}$ represents the mass-weighted average Mach number at the isolator exit. $T$ denotes the oscillatory period. For each time axis ($t_4$ or $t_5$), the zero point corresponds to the moment of the peak of an arbitrary chosen cycle at the corresponding PR condition.

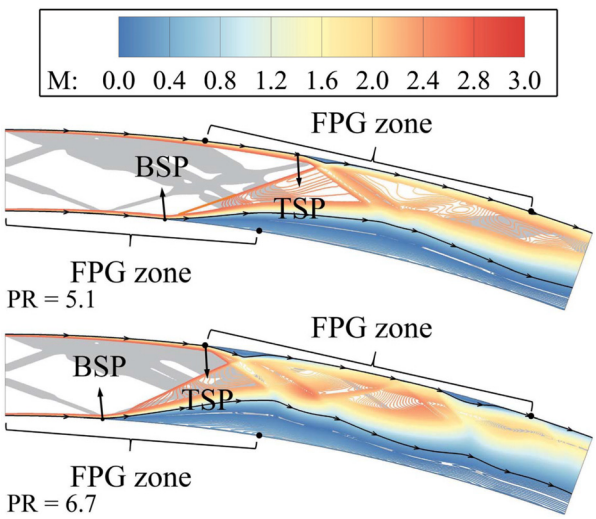


**FIG. 21.** Flow patterns at PRs of 5.1 and 6.7 (case I, phase IV).

experiences the final switch in the background pressure gradient from the outset and steps into the APG zone located most upstream along with the top leading shock. With increasing backpressure, the top separation continues extending forward rapidly, constantly pushing the shock toward the entrance. In contrast, the bottom branch of the leading shocks advances at a much gentler pace in the meantime. As a result, the asymmetry of the shock train is successively weakened, which is accompanied by a gradual conversion of the one-sided shock pattern into one similar to the cases at low PRs (e.g., Fig. 14). However, the bottom separation is still in the dominant position, and the supersonic core flow remains tilted toward the top wall until the end.

### B. Backpressure-dropping process and backpressure-induced hysteresis

Similar simulations and classifications are conducted on the backpressure-dropping process. Results show that there are also a total of five modes of transition adopted by the shock train, i.e., smooth movements, oscillations with an extreme asymmetric shock pattern,

the backward leap, oscillations with a slightly asymmetric shock pattern, and the disappearance of leading shocks. Overall, the whole course is basically an inversion of the foregoing backpressure-rising process, except for a marked difference arising at medium PRs. Considering this similarity and the limit of space, only a concise text description of each phase is provided in this section, and the remaining place is devoted to the discrepancy between the two processes.

#### 1. Phase I: Smooth movements (8.2 ≥ PR > 6.7)

Throughout this phase, the top and bottom separation points stay in the APG and FPG zones near the entrance, respectively. With a progressive decrease in backpressure, the shock train keeps retreating. Relatively speaking, there are much quicker variations of the top branch than those of the bottom branch in streamwise displacement and separation scale, which leads to the rapid intensification of flow asymmetry. Ultimately, the shock train evolves from crossed oblique shocks into a highly deflected structure.

#### 2. Phase II: Oscillations with an extremely asymmetric shock pattern (6.7 ≥ PR > 5.0)

When the PR is reduced to 6.8, the top separation moves back into an APG zone, and then the shock train starts to oscillate with an extremely asymmetric shock pattern derived from the previous phase. Similar unsteadiness can be observed afterward, provided the PR is higher than 5.0, except that the amplitude and frequency vary with the decreasing backpressure.

#### 3. Phase III: The backward leap (5.0 ≥ PR > 4.4)

When the PR drops to 5.0, the self-excited oscillations stop and the slowly downstream movement follows. Another change occurs amid the decrease in PR from 4.6 to 4.5: the shock train suddenly leaps far downstream. During this process, the bottom separation strides almost over an entire APG zone and shrinks sharply. In contrast, the distance that the top separation transfer is quite limited, and meanwhile, its size increases because the pushing effect from the other side weakens. This series of responses forces the shock train to return to a slightly asymmetric style.

#### 4. Phase IV: Oscillations with a slightly asymmetric shock pattern (4.4 ≥ PR > 3.4)

The bottom separation retreats into an FPG zone as the backpressure further reduces. Coincidentally, the top still lies in the FPG zone. Thereafter, the shock train becomes unstable again until the PR falls below 3.5. During this period, the shock train oscillates continually with a slightly asymmetric shock pattern. The amplitude and frequency follow a trend symmetric to that of the second phase in the backpressure-rising process.

#### 5. Phase V: The disappearance of leading shocks (3.4 ≥ PR > 1)

When the PR decreases to 3.4, the upper branch of the shock train moves back into the APG zone near the exit of the isolator, and the oscillations cease. At this time, only the leading shocks of the shock train remain entirely visible in the curved isolator. As backpressure further drops, the top shock continues moving downstream at a faster speed than BSP, taking the lead in vanishing. After that, only on the bottom wall exists the separation bubble, which shrinks further with the backpressure dropping. Ultimately, the shock train disappears completely, and an unpressurized flowfield same as Fig. 10 is presented.

Comparison between the backpressure-rising and -dropping processes indicates that their difference lies in the third phase, i.e., the forward/backward leap. For the backpressure-rising process, the onset of the abrupt shock-train leap follows the PR rising to 4.8. Interestingly, it is not until the PR descends to 4.5 that the inverted leap takes place. To better understand this phenomenon, Fig. 23 collects the flow pictures within this special pressure range. It is clear that there are actually two paths of development for the shock train, as can be also found in Fig. 24, where the curves of the bottom shock position are presented. Those two paths match perfectly in most cases, as analyzed above, and diverge only if the bottom shock gets close to the boundaries of the sole major APG zone on the bottom wall. Once inside the bifurcated region, the shock train depends strongly on the historical state. In short, a flow hysteresis happens. Fundamentally, it is an interesting phenomenon that can improve the knowledge of shock trains. For one thing, it proves that curved isolators can induce shock-train hysteresis by themselves, unlike straight isolators. For another, it demonstrates that isentropic waves are also capable of causing shock-train hysteresis. The underlying mechanism behind the phenomenon will be discussed in detail in Sec. VI.

### C. Relation between shock-train behaviors and local pressure gradients

Careful observation of the above-mentioned flow development shows that a reversal of the local pressure gradient tends to modify the behavioral pattern of the shock train in the kinematic or dynamic aspect. It suggests the strong and diverse effects of isentropic background waves on the shock-train state. From the flow modes exhibited in two pressure-varying processes, at least three sets of links can be discerned between local pressure gradients and shock-train behaviors, as detailed below.

(a) Situation 1: the separation point on each side stays in an FPG zone (corresponding to the second and fourth phases). In this case, self-excited oscillations of the shock train will take place. The closer the separation points to the middles of the FPG zones, the larger the amplitude.
(b) Situation 2: the top separation point is located in an FPG zone, while the bottom counterpart just enters or is about to enter an APG zone (corresponding to the third phase). This is a state when the shock train is extremely sensitive to downstream pressure. A slight pressure variation may cause a big and sharp shock-train leap as well as a radical transformation in the shock pattern.
(c) Situation 3: the top separation point lies in an APG zone, whereas the bottom counterpart is located in an FPG zone (corresponding to the first and fifth phases). In this situation, the shock train will be stable and vary smoothly with backpressure.

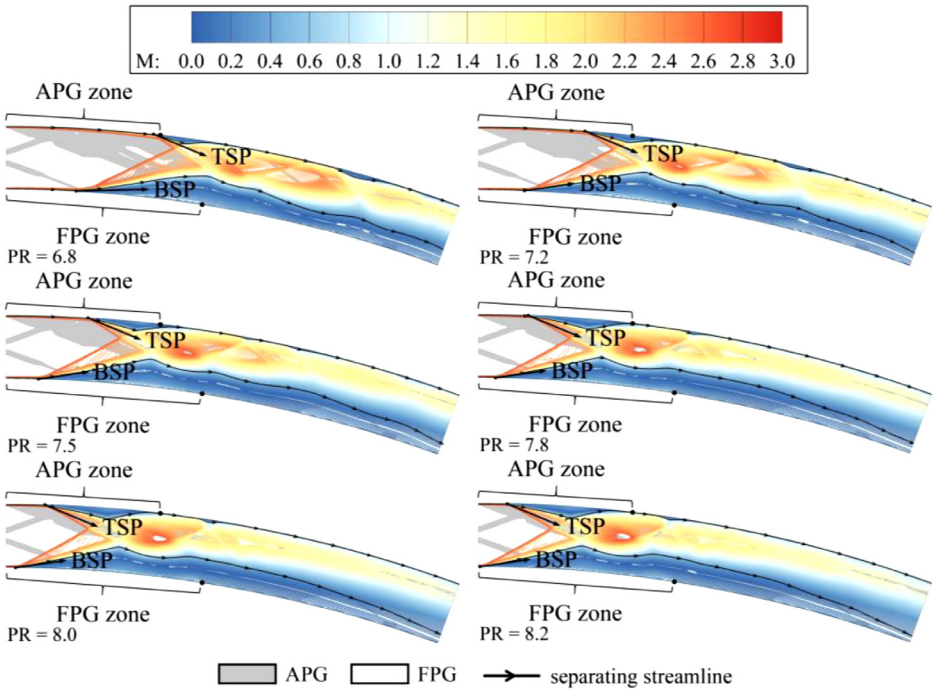


**FIG. 22.** Shock-train evolution during the fifth phase (case I, phase V, $6.7 < \mathrm{PR} \leq 8.2$).

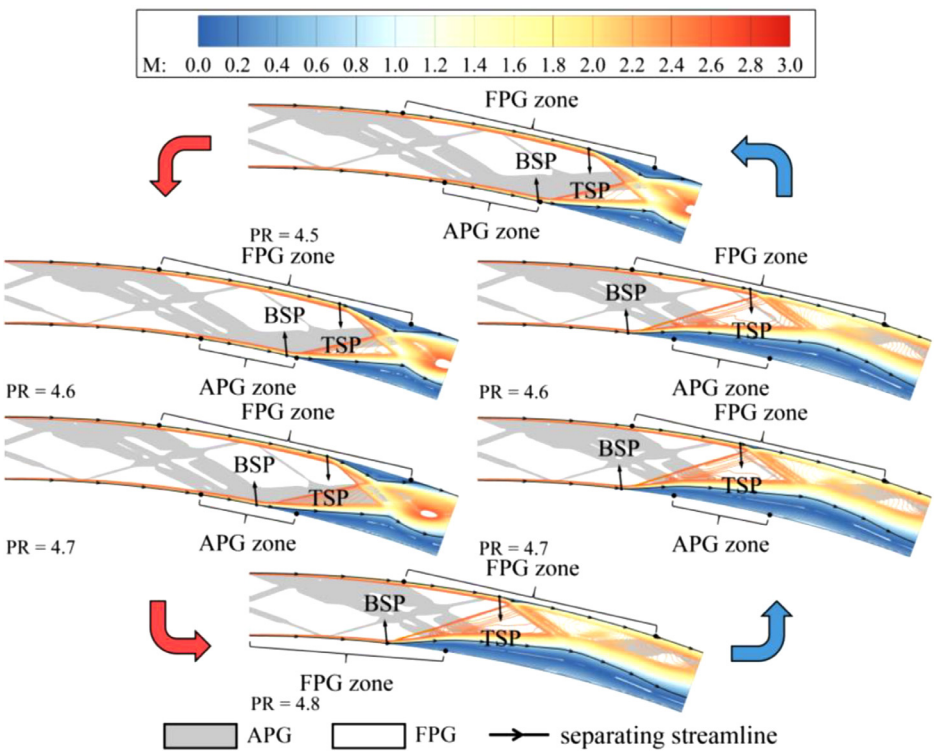


**FIG. 23.** Pressure-induced hysteresis of the shock train in the isolator (case I, phase III, $4.5 \leq \mathrm{PR} \leq 4.8$).

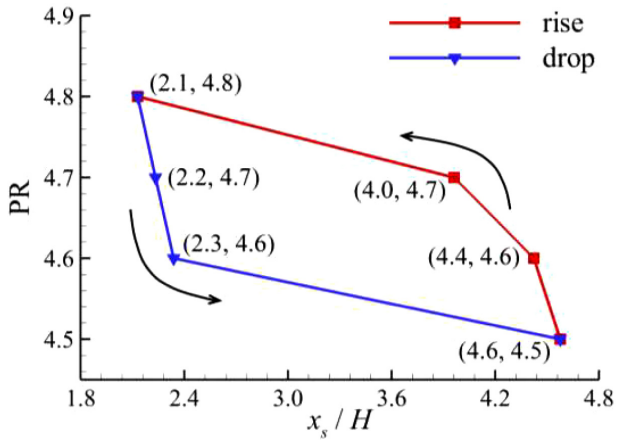


**FIG. 24.** Hysteresis loop of the leading shock positions at $h/H = 0$ (case I, phase III, $4.5 \leq \mathrm{PR} \leq 4.8$).

## V. EFFECTS OF CURVATURE ON SHOCK-TRAIN BEHAVIORS

The above results show that the shock-train behavior is somehow subject to the background pressure field created by the duct deflection. In this case, it is reasonable to infer that the behavior is prone to change with curvature. To reveal the curving effects, a detailed study is carried out on the isolators with angles of deflection of 10° and 30° (cases II and III in Table I), where the rest of the parameters are left unchanged. Their flow disparities will be introduced from the following two perspectives. The first part focuses on the general differences in shock-train development. The other is devoted to a close comparison of phenomena significantly affected by changing curvature.

### A. General differences in shock-train development

A similar classification is applied to the evolutionary development of new isolator flows. The corresponding PR ranges are collected in Tables III and IV along with the counterparts of case I. It can be seen that the development of the shock train at $\theta = 10°$ can also be divided into five flow phases, similar to that of the baseline model. Only the specific PR ranges differ between the two cases—the scopes of the second and fourth phases at $\theta = 10°$ narrow while the counterparts of the others expand. Relatively, a more complicated situation arises in the case of 30°. Apart from the contraction of the second and fourth phases, there is another phase of shock-train leap during the rise or decrease in backpressure. The new one occurs immediately after the formation of leading shocks or the end of shock oscillations in a slightly asymmetric style, depending on the direction of backpressure change. Compared with the original one, it features a smaller PR extent.

**TABLE III.** PR ranges of different flow phases in the backpressure-rising process.

| Phase | 10° | 20° | 30° |
|---|---|---|---|
| The appearance of leading shocks | (1, 3.8] | (1, 3.4] | (1, 2.9] |
| Oscillations with a slightly asymmetric shock pattern | (3.8, 4.5] | (3.4, 4.4] | (3.1, 3.9] |
| The forward leap | (4.5, 5.5] | (4.4, 5.0] | (2.9, 3.1], (3.9, 4.7] |
| Oscillations with an extremely asymmetric shock pattern | (5.5, 6.2] | (5.0, 6.7] | (4.7, 5.7] |
| Smooth movements | (6.2, 8.4] | (6.7, 8.2] | (5.7, 8.0] |

**TABLE IV.** PR ranges of different flow phases in the backpressure-dropping process.

| Phase | 10° | 20° | 30° |
|---|---|---|---|
| Smooth movements | [8.4, 6.2) | [8.2, 6.7) | [8.0, 5.7) |
| Oscillations with an extremely asymmetric shock pattern | [6.2, 5.5) | [6.7, 5.0) | [5.7, 4.7) |
| The backward leap | [5.5, 4.5) | [5.0, 4.4) | [4.7, 3.9), [3.1, 2.9) |
| Oscillations with a slightly asymmetric shock pattern | [4.5, 3.8) | [4.4, 3.4) | [3.9, 3.1) |
| The disappearance of leading shocks | [3.8, 1) | [3.4, 1) | [2.9, 1) |

Overall, with the increase in duct deflection, there is a tendency for the first phase in the backpressure-rising process (or the fifth phase in the inverse process) to be shortened. Meanwhile, the oscillations with a slightly asymmetric shock pattern and the forward/backward leap appear at smaller PRs, and the leap tends to occur with higher frequency. However, the extents of other flow phases show no clear trend with curvature. In addition, it can be noticed that the PR limit decreases with an increasing angle, which reflects that the resistance of the curved isolator to backpressure weakens when the curvature increases.

### B. Differences in behaviors of shock-train leap and hysteresis

The above analysis shows the most significant difference caused by curvature changes arises at medium PRs, where the forward and backward shock-train leaps are observed. Therefore, a detailed analysis is conducted below on this difference to further reveal the curvature effects. Considering the high correlation between the background pressure field and shock-train behaviors, the variations in the former one are first studied. The unpressurized flowfields and wall pressure distributions of isolators with angles of 10° and 30° are shown in Fig. 25. Combining it with Fig. 10, one can observe that the background pressure is clearly modified from the following two aspects. First, the amplitude, with which the wall pressure fluctuates streamwise, increases with duct deflection. Second, the APG zone becomes narrower. These two make local adverse pressure gradients intensify markedly. Additionally, unlike the other two cases, a left-running shock appears from the bottom APG zone when $\theta = 30°$, creating a nearly vertical pressure jump [circled in Fig. 25(b)].

The characteristics of shock-train leap and hysteresis change correspondingly under the influence of the background pressure field. Figures 26 and 27 show the shock trajectories and typical flow patterns at $\theta = 10°$, respectively, displaying a picture of the shock-train leap different from the case of 20° shown in Fig. 17. For one thing, it is not until the bottom separation goes deep into the APG zone that the forward shock-train leap is triggered. For another, technically, the bottom

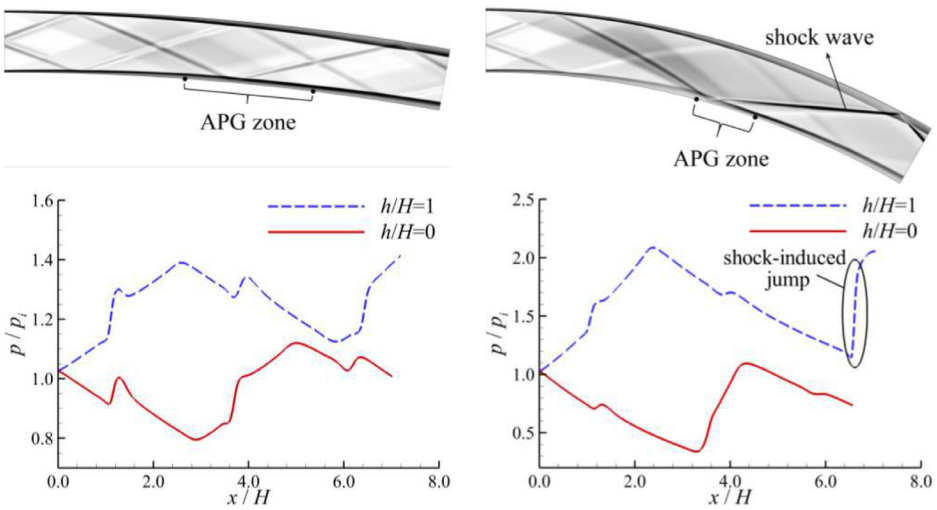


**FIG. 25.** Numerical schlieren images and wall-pressure distributions at the unpressurized state for isolators angled by (a) 10° (case II) and (b) 30° (case III).

separation does not overstep the upstream boundary of the APG zone yet after the leap ends, albeit almost. The later onset and earlier finish result in a smaller pace of the shock-train leap and variation in shock-train asymmetry, that is to say, a weaker leap phenomenon. Interestingly, a simulation of the backpressure-dropping process indicates the shock trains at PRs of 5.1 and 5.0 are exactly the same as the counterparts shown in Fig. 27, which gives an impression that no hysteresis exists in the 10° case. However, if reducing the backpressure step to 1/10 of the original (i.e., $\Delta p = 0.01 p_i$) and recalculating the process, one can find the hysteresis loop again (Fig. 28); it is just that the hysteresis is restricted to a very small pressure scope (PR = 5.01–5.05), which is also a reflection of the weakness of the current shock-train leap.

In contrast, intensification occurs in two dimensions when the angle of deflection turns into 30°. First, there is more than one leap, as mentioned earlier. It seems highly localized and the bottom branch of the shock train appears not to partake (Fig. 29). Observation further confirms that the newly emerging leap takes place along the top wall and in the vicinity of the incident point of the newly observed shock (Fig. 30). Compared with the one already found, the new one is weak in intensity. Consequently, the hysteresis that follows the leap is so faint that it can be detected only if the pressure step is reduced to 1/100 of the original or less, as shown in Fig. 31. Even so, the increase in the number of leaps reflects the leap-enhancing effect of higher curvature. Second, the leap coming up by the side of the bottom wall becomes more sensitive to the APG zone. As exhibited in Fig. 32, as soon as the leading shock touches the boundary of the APG zone, the leap happens (PR = 4.5–4.6). Furthermore, it is not until the leading shock moves far away from the APG zone that the leap stops. These make the leap feature a larger distance, and the accompanying hysteresis is aggravated accordingly.

To summarize, the increase in duct deflection significantly intensifies adverse pressure gradients and then the shock-train leap. Aside from that once the angle of deflection reaches a certain extent, one

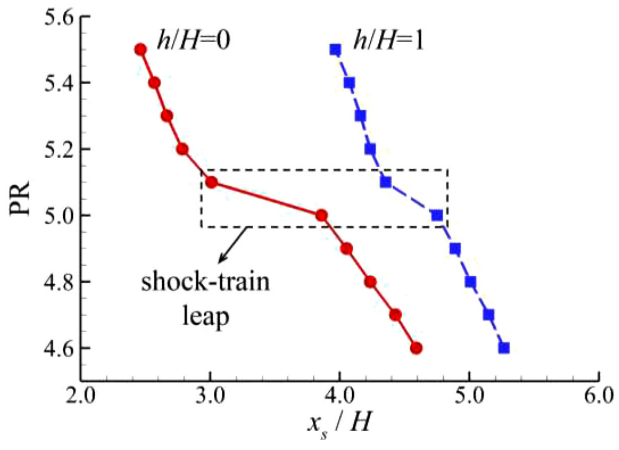


**FIG. 26.** Positional variations of leading shocks at the phase of the shock-train leap (case II, phase III, 4.6 ≤ PR ≤ 5.5).

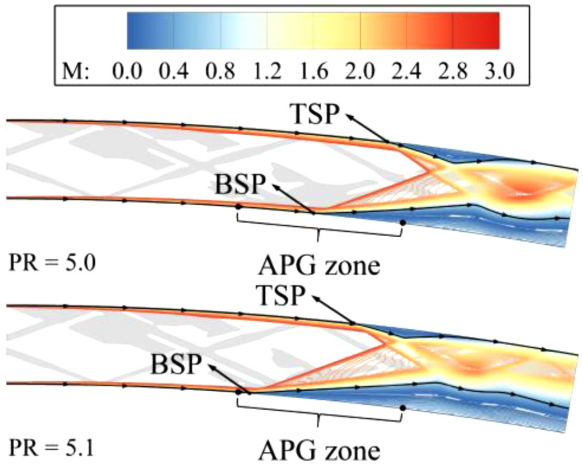


**FIG. 27.** Flow patterns before and after the shock-train leap (case II, phase III, PR = 5.0 and 5.1).

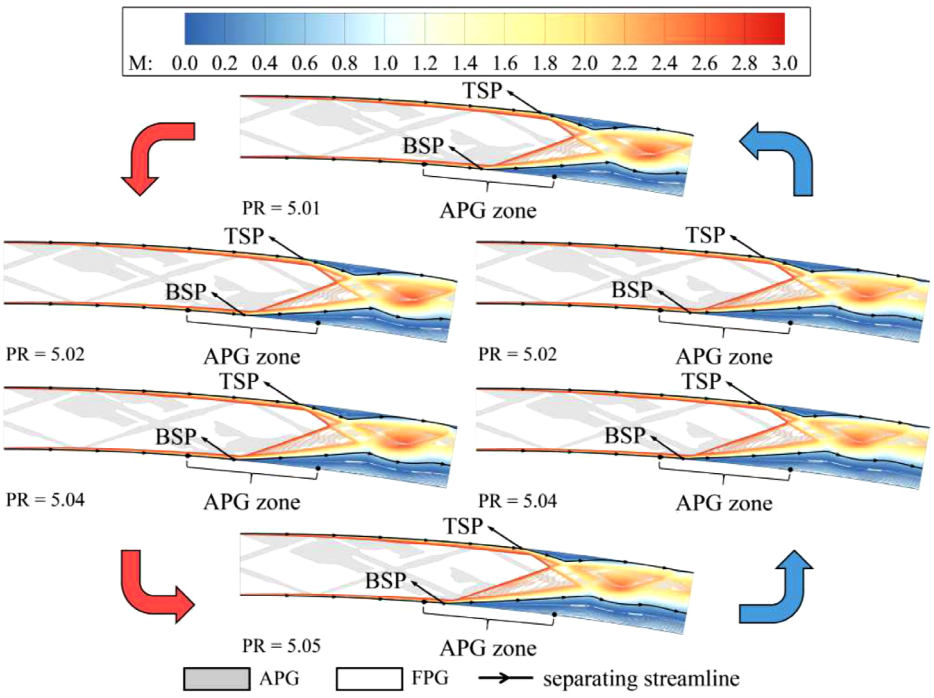


**FIG. 28.** Pressure-induced hysteresis of the shock train (case II, phase III, $5.01 \leq PR \leq 5.05$).

more leap and the attendant hysteresis loop may appear along the top wall. However, as far as this study is concerned, the shock-train leap and hysteresis of this kind are pretty weak and their impacts are expected to be limited.

## VI. DISCUSSION ON FLOW MECHANISMS IN CURVED ISOLATORS

### A. Autogenic pressure gradients and classifications of curved isolator flows

In a curved isolator, compression and expansion waves are produced by the concave and convex surfaces, respectively. Those waves intersect and yield a complex background, which has been already proven fairly influential to the shock train. In this case, addressing curved isolator flows requires the understanding of the autogenic waves' interaction and resultant pressure gradients.

Using the method of characteristics, Fig. 33 presents a typical inviscid pressure field at a freestream Mach number of 3 (case IV) to illustrate how a flow background is formed. It can be seen that the

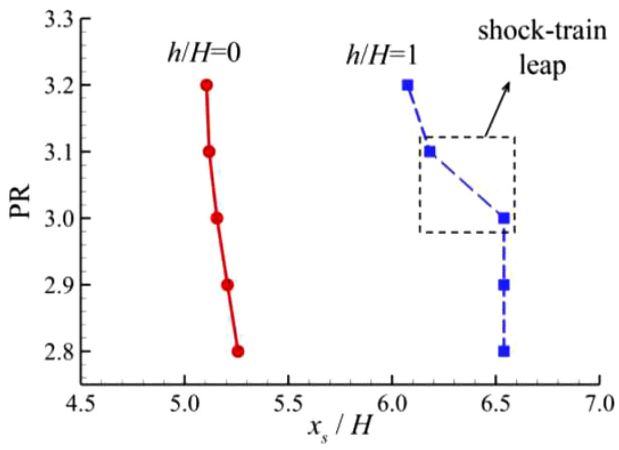


**FIG. 29.** Positional variations of leading shocks at the phase of the shock-train leap (case III, phase III, $2.8 \leq PR \leq 3.2$).

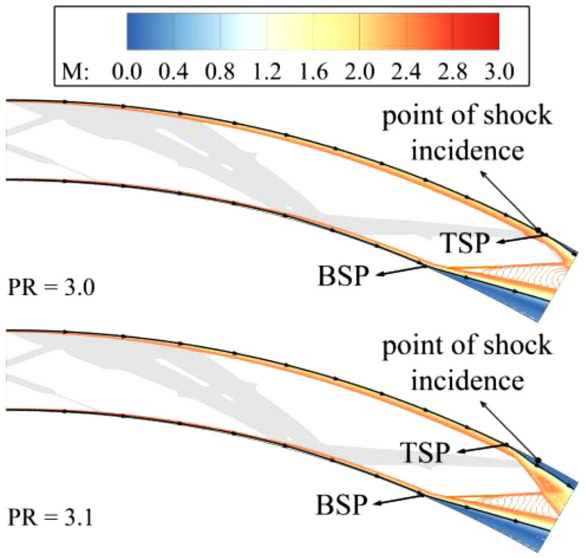


**FIG. 30.** Flow patterns before and after the shock-train leap (case III, phase III, PR = 3.0 and 3.1).

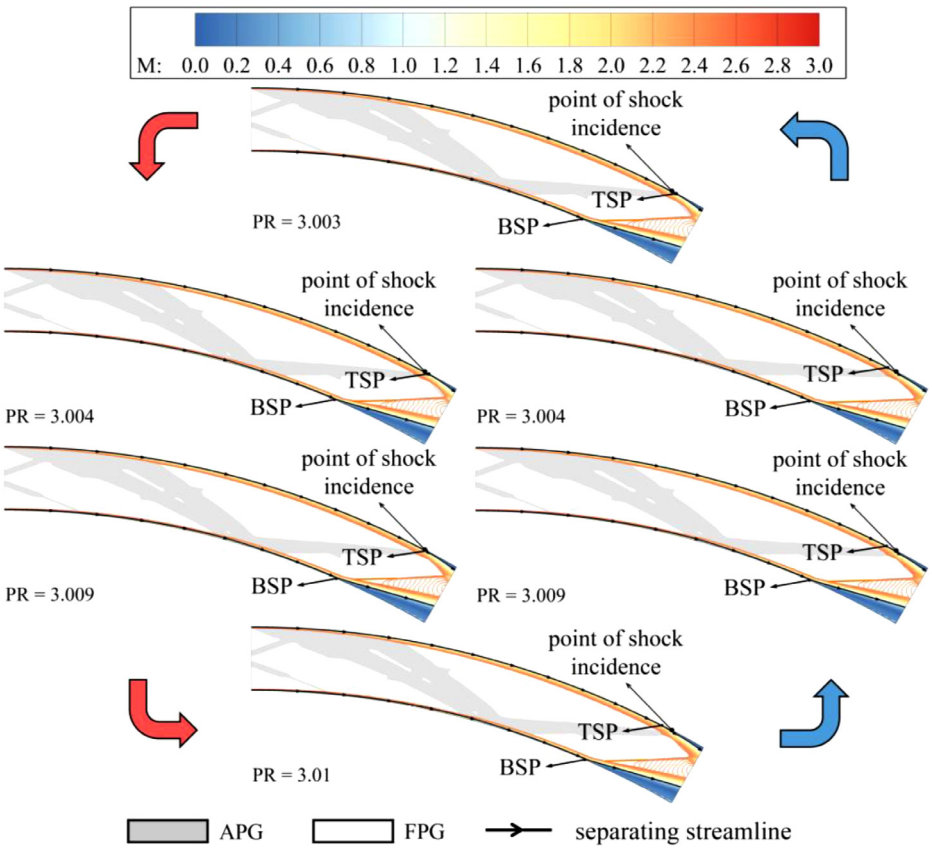


**FIG. 31.** Pressure-induced shock-train hysteresis within the PR range of 3.003–3.01 (case III, phase III).

wall-pressure curves fluctuate along the duct with roughly constant amplitude. Fundamentally, each cycle of a pressure uplift and fall is a result of one of the repeated processes in which two sorts of waves take effect by turns, as detailed below. Choosing the characteristic lines stemming from the entrance and their derivatives as boundaries, the flowfield segment included in Fig. 33 falls into seven portions, which are labeled A to G. Of them, A is a domain that remains undisturbed, thereby being fully uniform inside. B and F feature obviously an adverse streamwise pressure gradient, while C and E do exactly the opposite. In contrast, the situations in D and G are a little special. D is characterized by a radial pressure gradient, rather than a streamwise one. As for G, it can be inferred from the contour lines pointing approximately radially that a streamwise pressure change also exists there, and yet the slope is slight, which makes it resemble A to some degree. In terms of the underlying reason for the foregoing pressure distributions, there are four different mechanisms. The first one operates in parts B and C, where merely the isentropic waves induced by the adjacent wall are involved. Since there is only a single type of wave, the way the pressure varies naturally follows the attribute of the waves. The second one, which applies to part D, features a mixture of compression and expansion waves that originate from different families. Due to a similar effect on the radial pressure trend and a very opposite one on the streamwise counterpart, they offset each other streamwise and improve each other in the other direction, eventually resulting in a conspicuous radial pressure gradient. The third one, termed the wave-eliminating mechanism herein, works for the places such as E and F, which are usually located immediately downstream of a mixing region like the one just analyzed, portraying another way of the compression/expansion waves interaction. Taking region F as an example, there should have been two sets of waves, right-running compression waves and left-running expansion waves (or the reflected compression waves). Nevertheless, since the compression waves have a downward turning effect, its impingement makes the airflow locally parallel to the convex wall, suppressing both the generation of expansion waves and a reflection of compression waves. Consequently, the flow inside is under the total control of the incident compression waves and thereby suffers an adverse pressure gradient. It is the same when it comes to part E and it is just that the expansion waves play the part there. In other words, flows within E and F are actually determined by a single type of isentropic wave, similar to the cases of B and C. The difference is that the dominant waves are not generated by the wall nearby but from the other side. In engineering, a similar strategy is adopted to attenuate the reflection of the cowl-induced shock in a hypersonic inlet.[40] The last mechanism is applicable to parts A and G. While they look different, they share the same nature due to the aforementioned wave elimination in E and F, i.e., no wall-induced waves get directly involved. In this case, their flow characteristics depend totally on themselves. For the

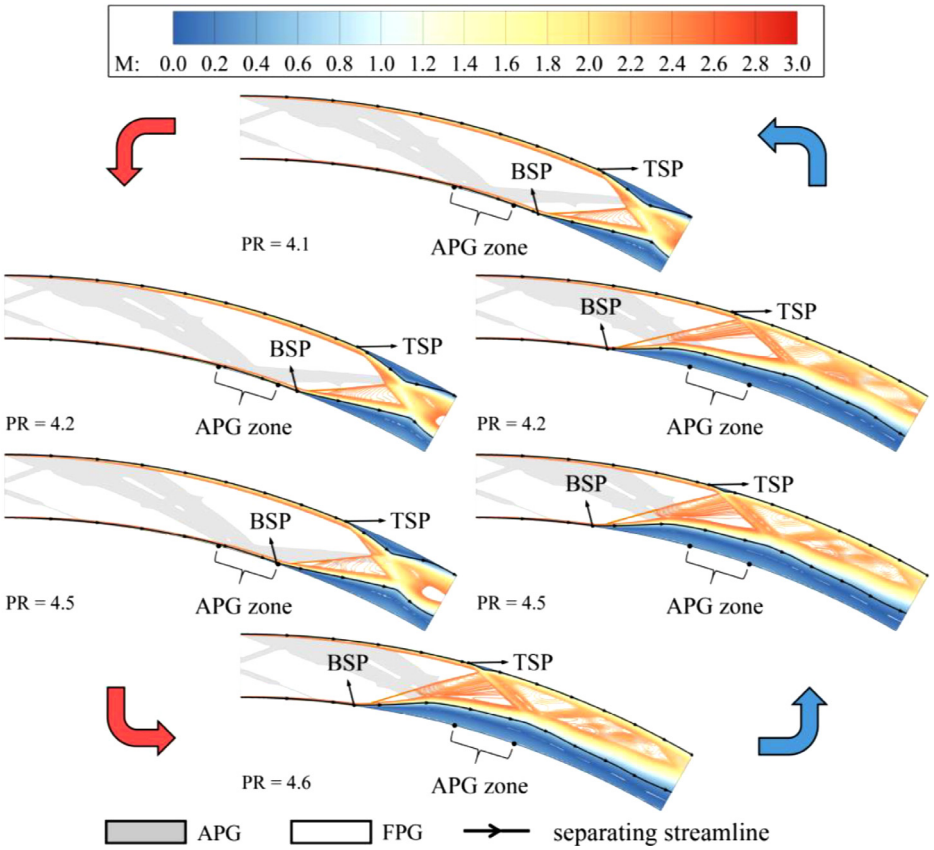


**FIG. 32.** Pressure-induced shock-train hysteresis within the PR range of 4.1–4.6 (case III, phase III).

case of A, the result is simple and there is no parameter variation in the whole area. As for G, the airflow at the upper boundary is slightly different in the degree of compression from the lower counterpart, which leads to the nonuniformity observed in Fig. 33. In its downstream regions, new isentropic waves will be produced, and then the foregoing cycle will repeat itself.

The existence of the areas like D complicates the analysis of the background flowfield within the whole space of a curved isolator, but if focusing on the near-wall regions, which are more critical to the shock-train characteristics, one may find out that there are just two alternative flow states for either side: one with the right-running compression waves and the other with the left-running expansion waves. This explains why the wall pressure always goes up and down repeatedly. However, it should be noted that each cycle is not a simple repeat of the previous. Owing to the bending of the duct and the inherent converging trend of compression waves, the extent that suffers the impact of compression waves narrows every time, and meanwhile, the scope of influence of expansion waves tends to expand [Fig. 33(a)]. This tendency causes an increasing slope of the pressure rise and a decreasing one of the pressure fall [Fig. 33(b)]. Conceivably, if the isolator were sufficiently long, there would be a moment when compression waves converge into a shock wave, as shown in Fig. 34(a). An extreme case can be also expected that the shock would take the place of the compression waves at the outset if the curvature of the isolator was strong enough [Fig. 34(b)]. Once this happens, the relevant flow regions, such as B, D, F, and G shown in Fig. 33(a), will all vanish and be replaced by a shock and its reflections. In this way, the pattern of background waves will transition from a combination of expansion waves and compression waves [Fig. 35(a)] to a shock-expansion waves' combination [Fig. 35(b)]. Their difference is that the latter features relatively strong adverse pressure gradients and an extra series of adverse pressure gradients traveling from the bottom up (corresponding to the new left-running shocks).

Based on the foregoing category of background waves, the curved isolator flows can be divided into two types from a general perspective. The first involves isolator flows dominated by compression and expansion waves, which roughly correspond to the cases weak in curvature or short in length. The second type is typical of ones dominated by shocks and expansion waves and is expected to be more common in isolators with strong curvature or long length. As far as the three cases studied in Secs. IV and V, the isolators with angles of deflection of 10° and 20° belong to the first type, while the remaining one is a mixture of two types. By the way, for isolators with shocks inherited from upstream hypersonic inlets, they can largely be treated as a second type owing to a similar wave composition (e.g., Fig. 10 in Ref. 22). Regarding this kind of isolator flow, extensive investigations have been conducted,[16,17,22,23] of which the conclusions we feel also apply to the second-type curved isolators with no inlet shocks, considering their close similarity. This is why this paper focuses its attention on the first-type flows.

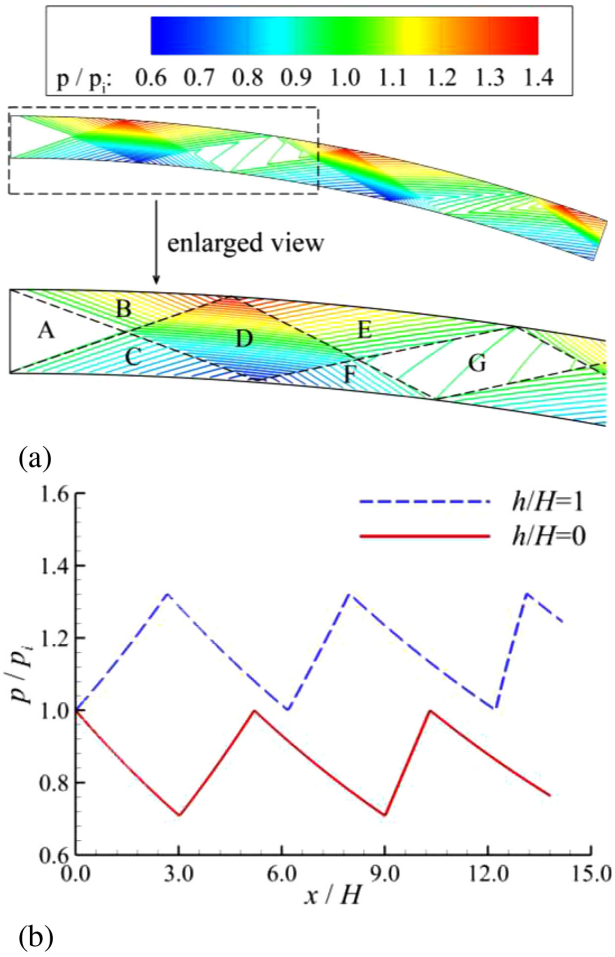


FIG. 33. Typical inviscid flow pattern in a curved isolator (case IV): (a) pressure contours; (b) wall-pressure distributions.

## B. Shock-train leap and hysteresis

In Sec. IV, we found the correspondence between shock-train positions and states. There are two phenomena of note, specifically, the self-excited oscillations, which occur when separation points on both sides stay in FPG zones, and the abrupt leap that arises when one of the separations enters an APG zone. Analysis indicates that all pressure gradients in the background are attributed to the inherent left-running expansion waves and right-running compression waves. Therefore, those phenomena fundamentally reflect two interesting flow problems: the shock-train instability under the influence of expansion waves and the nonlinear behavior of a shock train interacting with compression waves. Of them, the latter will be discussed below. As for the former, its mechanism is still unclear to us. Given its complexity and the limit of space, the analysis is left to the future.

To facilitate the understanding of the shock leap phenomenon, a sketch is provided in Fig. 36(a), which depicts the evolutionary process of separation after contact with a beam of compression waves. As the separation bubble moves from downstream into the scope of influence, a part of the compression waves interacts with it, increasing the

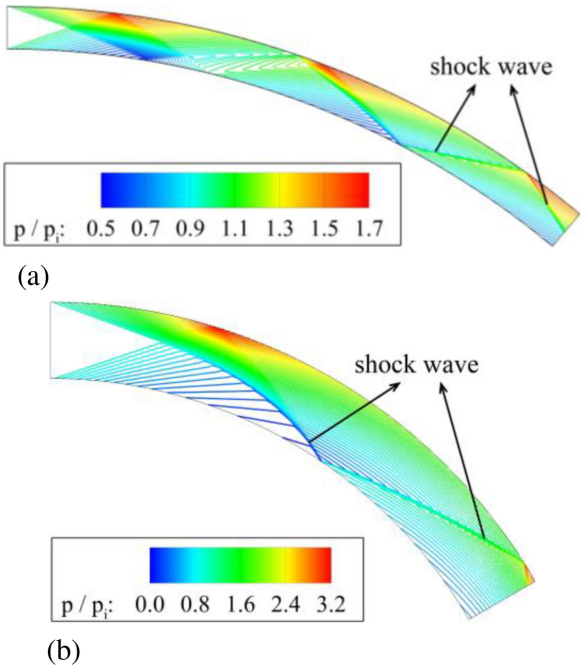


FIG. 34. Two ways of merging compression waves into shocks: (a) multiple reflections (case V); (b) strong curvature (case VI).

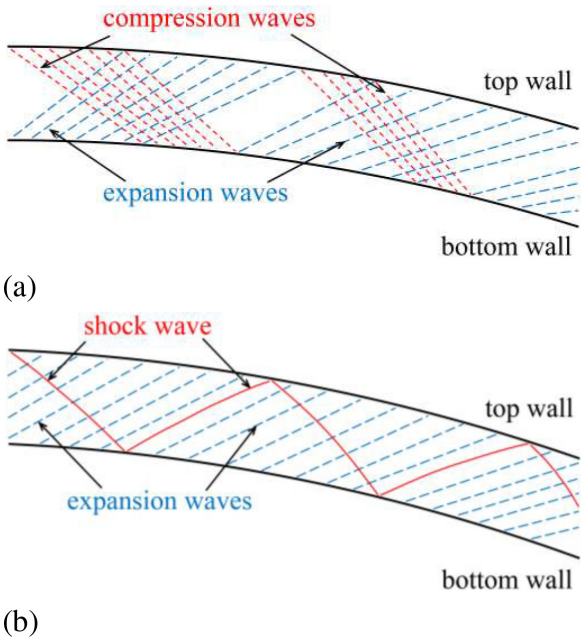


FIG. 35. Two types of autogenic background waves in curved isolators: (a) a combination of compression waves and expansion waves; (b) a combination of shock waves and expansion waves.

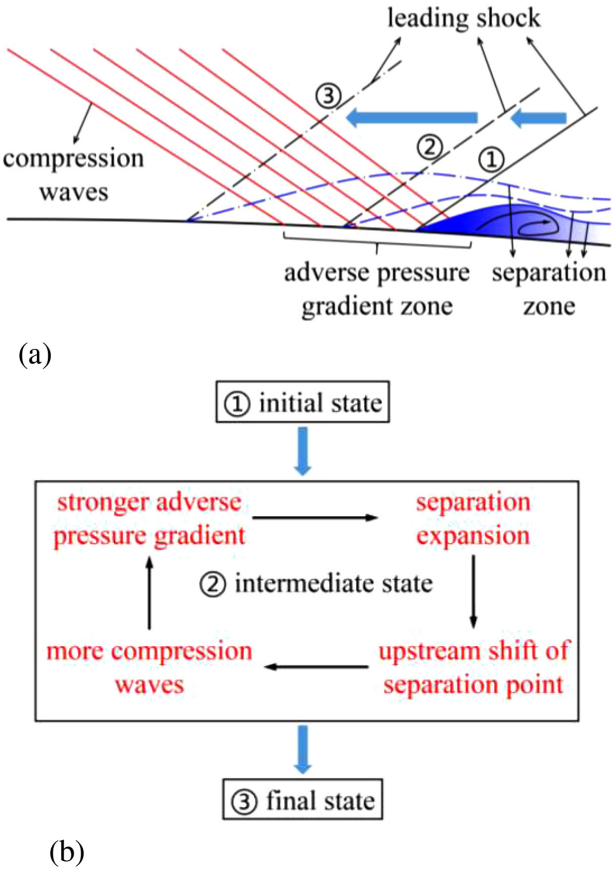


**FIG. 36.** Schematic diagrams illustrating the mechanism for the shock-train leap: (a) interaction between compression waves and a separation; (b) positive feedback loop.

pressure jump across the separation point. The separation cannot afford the added gradient, thereby extending upstream as a response to that. Subsequently, more compression waves participate in the interaction, which further aggravates the separation. In this way, a positive feedback loop is established, as described in Fig. 36(b). It renders the shock train highly sensitive and a slight backpressure increase can drive the separation and the leading shock to keep shifting upstream until the separation point completely leaves the area covered by the compression waves (cases I and III) or the remaining compression waves are too weak to affect a further change (case II), depending on the strength of incident compression waves. Either way, the interaction with compression waves makes it difficult for the separation to stand still, hence the occurrence of the forward shock-train leap. This mechanism guarantees a backward leap in the backpressure-dropping process as well. The reason is that only when the backpressure is adequately low can the influence of compression waves be fully offset and then can the separation make a complete retreat. Otherwise, the separation point would always stay upstream, as exemplified in Fig. 23. Furthermore, the existence of the two-way shock-train leap forces the shock train to follow a different path when the direction that the backpressure takes is reversed. This is why shock-train hysteresis happens. In other words, the shock-train leap and hysteresis are the cause and effect.

A comparison of the leap observed herein with the shock-induced leap reported previously in straight isolators reveals some similarities and differences. In a straight isolator with background shocks, it was found in Refs. 17–19 that the shock train often changed suddenly from a smooth movement state to a rapid movement state as the leading shock got close to the background shocks. This behavior agrees well with the observation in the present study, where a distinct case is considered. It indicates that the shock-train leap is likely to be a prevalent phenomenon for isolator flows, independent of isolator configurations and gradient types. This finding may help designers to make quick assessments during the design process. However, there are several minor differences in appearance between a shock-induced leap and one induced by compression waves, possibly because the gradient produced by compression waves is relatively mild in general. First, a shock-induced leap is often accompanied by shock-train oscillations,[17,21] which is not the case for the current investigation. Second, the shock train leaps on contact with an incident shock,[17] whereas it is normal for a compression wave-related case to have a buffer zone between the exposure to the incident waves and the onset of a leap. For instance, for the isolator with a 10° deflection, it is not until the shock train passed through roughly 50% of the impact area that a leap was triggered (Fig. 27).

Fundamentally, the delay in triggering reflects there is a minimum intensity threshold for an incident wave to provoke a shock-train leap. This is why the delay tends to expand as the curvature of the isolator weakens, and also why there are no shock-train leaps in straight isolators without background waves. Regarding the criterion, a review of the literature on isolator flows (e.g., Ref. 31) and relevant topics (e.g., Ref. 41) easily conveys an impression that the incident wave(s) should be strong enough to cause a flow separation by itself, given the fact that a local separation bubble can be usually observed in those studies. However, it seems not true for the current work. Figure 37 shows the friction coefficient distribution along the bottom wall of the baseline model, which operates at the unpressurized state. It can be seen that $C_f$ is always greater than zero, indicating that no separation is induced by the compression waves. It proves that a prior

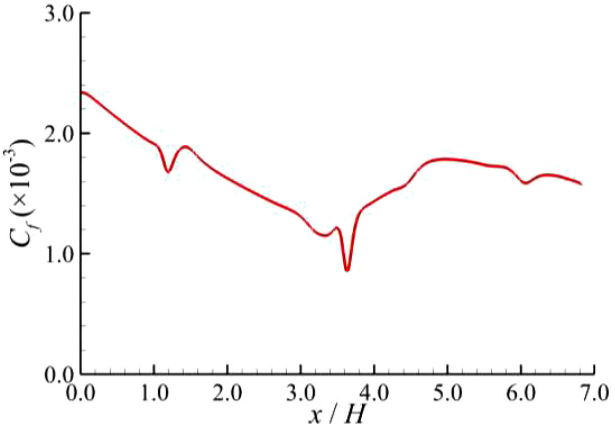


**FIG. 37.** Friction coefficient distribution along the bottom wall ($h/H = 0$) of the baseline model at the unpressurized state.

boundary-layer separation is not a prerequisite for a shock-train leap. Therefore, it can be speculated that the intensity threshold for an incident wave system to trigger a shock-train leap should lie below the critical value for separation.

## VII. CONCLUSIONS

A numerical study is conducted on the shock-train characteristics affected by inherent isentropic waves in simplified curved isolators. Results show that even without any shock or expansion wave from the inlet, adverse and favorable pressure gradients appear alternately along the duct walls due to the duct deflection. Under the influence of this complex background pressure field, the shock train presents up to five modes of transitions during a backpressure-varying process, namely, the appearance/disappearance of leading shocks, oscillations with a slightly asymmetric shock pattern, the abrupt leap, oscillations with an extremely asymmetric shock pattern, and smooth movements. Observation indicates that the advent of the shock-train oscillations and leaps is closely related to the local pressure distribution. The former occurs when the separation points on both sides stay in the domains featuring favorable pressure gradients, whereas the latter arises when one of the separations enters a region with an adverse pressure gradient. More interestingly, if the direction that the backpressure takes is reversed, the shock-train leap follows a different path of development, which leads to a shock-train hysteresis. When the curvature of the isolator increases from 10° to 30°, the leap phenomenon displays a tendency to grow in number and intensity and so does the related hysteresis. Meanwhile, the maximum backpressure a curved isolator can hold tends to decrease moderately.

An analysis based on the method of characteristics reveals that the formation of the background pressure field is attributed to the autogenic left-running expansion waves and right-running compression waves. They control the near-wall flow state by turns due to the wave-eliminating effect, resulting in cyclic changes in the local pressure gradient sign. However, each cycle is not a simple repeat of the previous. Owing to the bending of the duct and the inherent converging trend of compression waves, the space of the compression waves narrows gradually. If the isolator is adequately curved or long, compression waves will be replaced with shocks in the end. In this case, curved isolator flows can be roughly classified into two categories according to the pattern of background waves; one features a combination of expansion and compression waves, whereas the other is characterized by a combination of shocks and expansion waves.

Further analysis indicates that the interaction between incident compression waves and separation can establish a positive feedback mechanism, which makes it difficult for the shock train to stand still under the compression waves. Accordingly, the shock train becomes highly sensitive and a slight backpressure change can force the shock train to leap and deform suddenly when there are compression waves, backward or forward, which further contributes directly to the appearance of flow hysteresis. Comparison with the shock-induced leap reported previously shows that there is a marked similarity in their behaviors, despite the clear distinctions in the model configuration and the form of incident waves. It suggests that the shock-train leap is likely to be prevalent among isolator flows. Nevertheless, unlike a shock-related case, no attendant flow oscillations follow a leap induced by compression waves, and its onset is often delayed, possibly because of the natural dispersion of compression waves. Fundamentally, the latter change reflects that there is a minimum intensity threshold for an incident wave to trigger a shock-train leap. Given the fact that no prior separation is provoked by the compression waves, it is speculated that the threshold should actually lie below the criterion for separation, as opposed to the impression given by the previous research.

## ACKNOWLEDGMENTS

This work was funded by the National Natural Science Foundation of China (Grant Nos. 12102440, U2141220, and 11902325). The authors sincerely thank two anonymous referees for their helpful suggestions.

## AUTHOR DECLARATIONS

### Conflict of Interest

The authors have no conflicts to disclose.

### Author Contributions

**Li-hao He:** Formal analysis (lead); investigation (lead); writing – original draft (lead). **Hao Chen:** Conceptualization (lead); funding acquisition (supporting); writing – review & editing (lead). **Lian-jie Yue:** Funding acquisition (lead); supervision (lead). **Qi-fan Zhang:** Funding acquisition (supporting); methodology (lead). **Wan-nan Wu:** Validation (lead).

## DATA AVAILABILITY

The data that support the findings of this study are available from the corresponding author upon reasonable request.

## REFERENCES

[1]M. K. K. Devaraj, P. Jutur, S. M. V. Rao *et al.*, "Experimental investigation of unstart dynamics driven by subsonic spillage in a hypersonic scramjet intake at Mach 6," Phys. Fluids **32**, 026103 (2020).
[2]W. H. Heiser, D. T. Pratt, D. H. Daley *et al.*, *Hypersonic Airbreathing Propulsion* (AIAA, 1994).
[3]E. T. Curran and S. N. B. Murthy, *Scramjet Propulsion* (AIAA, 2001), Vol. 189.
[4]K. Matsuo, Y. Miyazato *et al.*, "Shock train and pseudo-shock phenomena in internal gas flows," Prog. Aerosp. Sci. **35**(1), 33–100 (1999).
[5]F. Gnani, H. Zare-Behtash, and K. Kontis, "Pseudo-shock waves and their interactions in high-speed intakes," Prog. Aerosp. Sci. **82**, 36–56 (2016).
[6]R. Saravanan, S. Desikan, and T. M. Muruganandam, "Isolator characteristics under steady and oscillatory back pressures," Phys. Fluids **32**(9), 096104 (2020).
[7]Z. Wang, J. Chang, G. Wu *et al.*, "Experimental investigation of shock train behavior in a supersonic isolator," Phys. Fluids **33**(4), 046103 (2021).
[8]E. T. Curran, "Scramjet engines: The first forty years," J. Propul. Power **17**(6), 1138–1148 (2001).
[9]P. J. Waltrup, M. E. White, F. Zarlingo *et al.*, "History of U.S. Navy ramjet, scramjet, and mixed-cycle propulsion development," J. Propul. Power **18**(1), 14–27 (2002).
[10]L. H. Townend, "Domain of the scramjet," Philos. Trans. R. Soc. A **357**(1759), 2317–2334 (1999).
[11]N. Li, J. Chang, K. Xu *et al.*, "Oscillation of the shock train in an isolator with incident shocks," Phys. Fluids **30**(11), 116102 (2018).
[12]C. Kong, J. Chang, Y. Li *et al.*, "A deep learning approach for the velocity field prediction in a scramjet isolator," Phys. Fluids **33**(2), 026103 (2021).
[13]N. Li, "Reciprocating and flapping motions of unstart shock in a scramjet isolator," Phys. Fluids **34**(1), 016102 (2022).
[14]Z. Wang, J. Chang, Y. Li *et al.*, "Oscillation of the shock train under synchronous variation of incoming Mach number and backpressure," Phys. Fluids **34**, 046104 (2022).

[15]V. R. P. Sethuraman, Y. Yang, and J. G. Kim, "Low-frequency shock train oscillation control in a constant area duct," Phys. Fluids **34**, 016105 (2022).
[16]H. Tan, S. Sun, and H. Huang, "Behavior of shock trains in a hypersonic inlet/isolator model with complex background waves," Exp. Fluids **53**(6), 1647–1661 (2012).
[17]K. Xu, J. Chang, W. Zhou *et al.*, "Mechanism and prediction for occurrence of shock-train sharp forward movement," AIAA J. **54**(4), 1403–1412 (2016).
[18]K. Xu, J. Chang, W. Zhou *et al.*, "Mechanism of shock train rapid motion induced by variation of attack angle," Acta Astronaut. **140**, 18–26 (2017).
[19]K. Xu, J. Chang, N. Li *et al.*, "Experimental investigation of mechanism and limits for shock train rapid forward movement," Exp. Therm. Fluid Sci. **98**, 336–345 (2018).
[20]N. Li, J. Chang, D. Yu *et al.*, "Mathematical model of shock-train path with complex background waves," J. Propul. Power **33**(2), 468–478 (2017).
[21]N. Li, J. Chang, K. Xu *et al.*, "Prediction dynamic model of shock train with complex background waves," Phys. Fluids **29**(11), 116103 (2017).
[22]H. Huang, H. Tan, S. Sun *et al.*, "Unthrottled flows with complex background waves in curved isolators," AIAA J. **55**(9), 2942–2955 (2017).
[23]H. Huang, H. Tan, S. Sun *et al.*, "Behavior of shock train in curved isolators with complex background waves," AIAA J. **56**(1), 329–341 (2018).
[24]W. Hou, J. Chang, Z. Xie *et al.*, "Behavior and flow mechanism of shock train self-excited oscillation influenced by background waves," Acta Astronaut. **166**, 29–40 (2020).
[25]W. Hou, J. Chang, Y. Wang *et al.*, "Experimental study on the forced oscillation of shock train in an isolator with background waves," Aerosp. Sci. Technol. **106**, 106129 (2020).
[26]Z. Wang, J. Chang, W. Hou *et al.*, "Low-frequency unsteadiness of shock-wave/boundary-layer interaction in an isolator with background waves," Phys. Fluids **32**(5), 056105 (2020).
[27]T. Huang, L. Yue, S. Ma *et al.*, "Downstream pressure variation induced hysteresis in the scramjet isolator," AIAA Paper No. 2017-2436, 2017.
[28]X. Jiao, J. Chang, Z. Wang *et al.*, "Periodic forcing of a shock train in a scramjet inlet-isolator at overspeed condition," Acta Astronaut. **143**, 244–254 (2018).
[29]W. Shi, J. Chang, J. Ma *et al.*, "Path dependence characteristic of shock train in a 2D hypersonic inlet with variable background waves," Aerosp. Sci. Technol. **86**, 650–658 (2019).
[30]T. Huang, Q. Zhang, L. Yue *et al.*, "Hysteresis of shock train movement in the isolator with a ramp," AIAA J. **59**(10), 3873–3882 (2021).
[31]N. Li and J. Chang, "Hysteretic behaviors of separation-shock driven by backpressure in isolator with incident shocks," AIAA J. **59**(3), 960–971 (2021).
[32]B. Xiong, X. Fan, Z. Wang *et al.*, "Analysis and modelling of unsteady shock train motions," J. Fluid Mech. **846**, 240–262 (2018).
[33]K. R. Sekar, S. K. Karthick, S. Jegadheeswaran *et al.*, "On the unsteady throttling dynamics and scaling analysis in a typical hypersonic inlet-isolator flow," Phys. Fluids **32**(12), 126104 (2020).
[34]H. Huang, H. Tan, S. Sun *et al.*, "Evolution of supersonic corner vortex in a hypersonic inlet/isolator model," Phys. Fluids **28**(12), 126101 (2016).
[35]F. R. Menter, "Two-equation eddy-viscosity turbulence models for engineering applications," AIAA J. **32**(8), 1598–1605 (1994).
[36]B. F. Carroll and J. C. Dutton, "Characteristics of multiple shock wave/turbulent boundary-layer interactions in rectangular ducts," J. Propul. Power **6**(2), 186–193 (1990).
[37]K. Kawatsu, S. Koike, T. Kumasaka *et al.*, "Pseudo-shock wave produced by back pressure in straight and diverging rectangular ducts," AIAA Paper No. 2005-3285, 2005.
[38]J. L. Wagner, K. B. Yuceil, A. Valdivia *et al.*, "Experimental investigation of unstart in an inlet/isolator model in Mach 5 flow," AIAA J. **47**(6), 1528–1542 (2009).
[39]Z. Li, W. Gao, H. Jiang *et al.*, "Unsteady behaviors of a hypersonic inlet caused by throttling in shock tunnel," AIAA J. **51**, 2485–2492 (2013).
[40]N. O. Prakash Raj and K. Venkatasubbaiah, "A new approach for the design of hypersonic scramjet inlets," Phys. Fluids **24**(8), 086103 (2012).
[41]Y. Hu, W. Zhou, G. Wang *et al.*, "Bistable states and separation hysteresis in curved compression ramp flows," Phys. Fluids **32**(11), 113601 (2020).